Spring 5-13-2023

ELECTROCHEMICAL PROPERTIES OF MOF-DERIVED NICKEL COMPOUNDS FOR HIGH-PERFORMANCE SUPERCAPACITORS AND ELECTROCATALYSTS

Shiva Bhardwaj
Pittsburg State University, shiva.bhardwaj@gus.pittstate.edu

Recommended Citation

Bhardwaj, Shiva, "ELECTROCHEMICAL PROPERTIES OF MOF-DERIVED NICKEL COMPOUNDS FOR HIGH-PERFORMANCE SUPERCAPACITORS AND ELECTROCATALYSTS" (2023). *Electronic Theses & Dissertations*. 443.
https://digitalcommons.pittstate.edu/etd/443

ELECTROCHEMICAL PROPERTIES OF MOF-DERIVED NICKEL COMPOUNDS FOR HIGH-PERFORMANCE SUPERCAPACITORS AND ELECTROCATALYSTS

A Thesis Submitted to the Graduate School
in Partial Fulfillment of the Requirements
For the Degree of
Master of Material Science

Shiva Bhardwaj

Pittsburg State University

Pittsburg, Kansas

May, 2023

ELECTROCHEMICAL PROPERTIES OF MOF-DERIVED NICKEL COMPOUNDS FOR HIGH-PERFORMANCE SUPERCAPACITORS AND ELECTROCATALYSTS

Shiva Bhardwaj

APPROVED:

Thesis Advisor ______________________________
Dr. Ram K. Gupta, Department of Chemistry

Committee Member ______________________________
Dr. Serif Uran, Department of Physics

Committee Member ______________________________
Dr. Khamis Siam, Department of Chemistry

Acknowledgments

I want to express my sincere gratitude to Dr. Ram K. Gupta for overseeing me and providing many helpful suggestions. His commitment, focus, and critical thinking greatly encouraged me for the research job. He has played a significant role in my academic and research courses by suggesting what course to choose for the perfect semester. I want to acknowledge Dr. Khamis Siam and Dr. Serif Uran for accepting my invitation to serve as my thesis committee member and taking time away from their important schedule.

I want to thank Felipe M. DeSouza for providing extensive knowledge of writing chapters and research articles. Also, he helped me in taking the SEM and EDS images of my samples to support my thesis and research work.

Also deserving of praise are Pittsburg State University and the National Institute for Materials Advancement (NIMA), who funded my research work and allowed me to use all instruments. It also encouraged me to attend conferences and present my work locally and nationally.

I want to thank my father, Mr. Dinesh Bhardwaj, and my mother, Mrs. Savita Bhardwaj, for encouraging me to come to the United States for higher education. Also, thanks to my siblings, who are a great source of motivation for me. I'm grateful that my family members recognize my accomplishments, inspiring me to work harder.

Ultimately, I would like to thank all my colleagues with whom I have worked and with whom I’m currently working at NIMA.

ELECTROCHEMICAL PROPERTIES OF MOF-DERIVED NICKEL COMPOUNDS FOR HIGH-PERFORMANCE SUPERCAPACITOR AND ELECTROCATALYSTS

An Abstract of the Thesis by
Shiva Bhardwaj

There are various forms in which humans use energy in daily life. From applications that require a high energy density to long-term storage, the requirements for energy usage are diverse. Therefore, with the continuous increase in users worldwide, more practical energy-driven sources are required, allowing manufacturers to look toward emerging functional materials. An emerging class of functional porous materials referred to as metal-organic framework (MOF) has received considerable attention over the past two decades, partially because of their potential use in various applications, including gas storage, molecular separations, electrocatalyst, and energy devices. For example, metal oxide and hydroxide-based MOF materials are widely used for supercapacitor (SC) and electrocatalyst applications.

This thesis aims to study the electrochemical properties of nickel-derived oxide and hydroxide-based MOF for application in SCs and electrocatalysts. The effect of growth temperature on the electrochemical properties of these samples were studied. To tune the surface area and porosity, these MOFs were prepared at different temperatures. Nickel acetate and glutaric acid were used as main precursors in synthesizing nickel hydroxide (NH)-MOF (NH-MOF-140, 160, and 180 °C) and nickel oxide (NO)-based MOF (NO-MOF-140, 160, and 180 °C) at various temperatures. The as-prepared NH and NO-MOFs were analyzed using various techniques. Scanning electron microscopy (SEM) and X-ray diffraction (XRD) determined the microstructure and phases of the derived hydroxides and

oxides. As a result, the NH-MOF-160 shows the highest specific capacitance (C_{sp}) of 608 F/g along with 3.98 kW/kg and 24.92 Wh/kg of power and energy density, respectively. Also, the NH-MOF-160 shows the lowest overpotential of 268 mV for oxygen evolution reaction (OER) and 176 mV for hydrogen evolution reaction (HER) to reach a current density of 10 mA/cm^2.

TABLE OF CONTENTS

LIST OF TABLES

LIST OF FIGURES

CHAPTER I

INTRODUCTION

1.1 Need for energy storage and production

An energy storage system (ESS) works by capturing energy produced and using it later to maintain the balance between energy demand and production [1]. The energy storage sector has been working toward ESSs to meet current and future demand for energy. Rapid advancement in the energy storage sector, coupled with significant increase in the global population, has led to increased demand for energy. It is also important to develop renewable energy sources to lower the carbon emissions produced by burning fossil fuels, the current primary energy source in industries today. ESS can provide a rich spectrum of benefits [2]. ESS provides grid flexibility to ensure that consumers always have access to electricity, regardless of its uses. This flexibility is necessary for both dependability and resilience. As outage costs continue to rise, the value of increased resilience and reliability also increases [3].

1.2 Devices used for energy storage and production

The devices used for ESS are referred to as accumulators [4]. This is because they allow quick energy intake over a short period of time and release energy when needed. Accumulators typically store energy in various forms like thermal, mechanical, chemical, and electrical energy. Some examples of accumulators include flywheel energy storage, inductors, pumped-storage hydroelectric (PSH) plants, rechargeable batteries, supercapacitors, and fuel cells [5]. **Figure 1(a-e)** shows different types of accumulators.

A flywheel accelerates and stores energy as rotational energy and works on the principle of energy conservation. In contrast, an inductor stores energy in the form of a magnetic field and works on the principle of Faraday's law of induction [6]. PSH stores energy in hydroelectricity and works on the principle of gravitational potential energy. Rechargeable batteries store energy chemically and work on the principle of electrochemistry [7]. SC stores energy in different forms, electrically and electrochemically, and finally, fuel cells work on the redox reaction mechanism and convert the chemical energy of the fuel to electricity [8].

Industrial flywheels are used for operational rockets by the National Aeronautics and Space Agency (NASA); however, they are expensive. In contrast, the PSH and inductor have limited practical applications. Therefore, researchers look towards rechargeable batteries as they possess a high energy density; however, they cannot generate the sudden power required for photographic flashes in digital camera for such a short time period of 90 sec. The benefit of SC as ESS is that they can provide a better power density and efficiency in a long run cycle and are comparatively cheaper than batteries [9]. To tackle net zero carbon emission, scientists look towards a new ESS called fuel cells (FC). Herein, we are focusing on SC and FC-based ESS. **Figure 1(f)** shows a comparison between various devices available in the market.

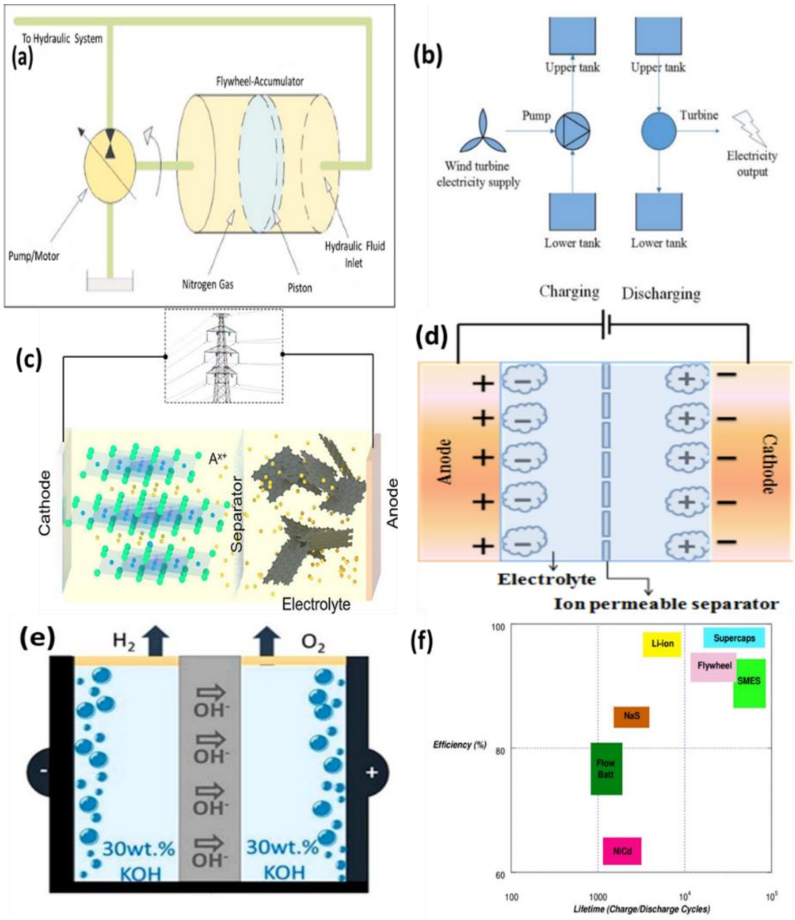

Figure 1: Schematic of different accumulators (a) flywheel “Adapted with permission [10]. Copyright (2016) SAGE”. This article is distributed under the term of the creative commons attribution 3.0 license which permits any use, reproduction, and distribution of work without further permission. (b) PSH system “Adapted with permission [1]. Copyright (2020) Elsevier” (c) rechargeable battery “Adapted with permission [5]. Copyright (2022) American Chemical Society” (d) SC “Adapted with permission [11], Copyright (2021) American chemical Society” (e) FC “ Adapted with permission [12]. Copyright (2022) National Research Council of Canada. Published by American Chemical Society” with common creative attribution 4.0 license which permits free distribution; and (f) compares the efficiency percentage and life cycle of different ESS. “Adapted with permission [13]. Copyright (2008) Elsevier”.

1.3 Basics of supercapacitors

The history of the capacitor starts with the Leyden jar, invented in the middle of the 18th century by Dutch and German scientists. Using this invention, they developed the concept of storing electrical charges electrostatically [14]. Nearly 100 years ago, Von-Helmholtz was the first to propose an electrostatic charge storage mechanism. **Figure 2(a)** represents the history of capacitors from the Leyden jar to asymmetric SC. In 1910, Gouy-Chapman proposed the diffusion of ions into a solution of electrolyte and the diffused space, termed as diffusive layer [15]. In 1924, Stern and Grahame modified the Gouy-Chapman model. Stern stated that there are two layers on the surface of the electrode, an adsorbed layer (Helmholtz layer) and a diffusive layer (Gouy-Chapman model) [16]. In 1971, researchers discovered a new type of capacitance phenomenon called pseudocapacitance. This enhances the charge-storing capability of capacitors. In 1989, the U.S. Department of Energy initiated the SC development program, which led to a dramatic increase in the number of researchers and the invention of asymmetric and hybrid SC [17]. The significant difference between capacitors and SC is the energy storage capacity. A SC generally works on two phenomena based on its charge storage mechanism: electric double-layer capacitance (EDLC) and pseudocapacitance.

Electric double layer capacitance works on a non-faradaic charge storage mechanism process, meaning an adsorption and desorption mechanism occurs. This is the surface phenomenon. EDLC was first discovered by Helmholtz, who found a double-layer formation at the electrode's surface in the 1970s [18]. Furthermore, Gouy-Chapman discovered that the ions moving to and fro between the electrode and electrolyte creates some diffused space, referred to as a diffused layer formed due to the diffusion of ions.

Moreover, Stern and Grahame modified the Helmholtz and Gouy-Chapman model. Stern identified two different regions between electrode and electrolyte: the 1st layer is due to adsorption and desorption phenomena, as shown in **Figure 2(b)**, and 2nd layer is referred to as the diffusive layer [19]. Grahame studied the Helmholtz plane and divided it into two sub-categories (a) inner Helmholtz plane (IHP) and (b) outer Helmholtz plane (OHP). These planes correspond to the difference in the closest approach, which may arise due to the difference in the radii of cations and anions. They also retain solvation shells due to strong ion-solvent dipole interactions [20].

Pseudocapacitance involves fast reversible redox reactions near the electrode surface or intercalation/de-intercalation of ions at the electrode surface, i.e., it works on the faradaic process. SCs showing this phenomenon are called pseudocapacitors, which show three types of processes (**Figure 2(c)**): underpotential deposition, surface redox reactions, and intercalation.

Underpotential deposition refers to the deposition of ions on the electrode-electrolyte interface that usually takes place during noble metal adsorption as well as deposition of cations for reduction and can be described in equation 1 as follows:

$$M + xC^{z+} + xZe^{-} \rightleftharpoons CM \qquad \text{eq. 1}$$

where C is the adsorbed atoms, M is the noble metal, x is the number of adsorbed atoms, z is the valency of an adsorbed atom, and xZ is the transferred electrons [21].

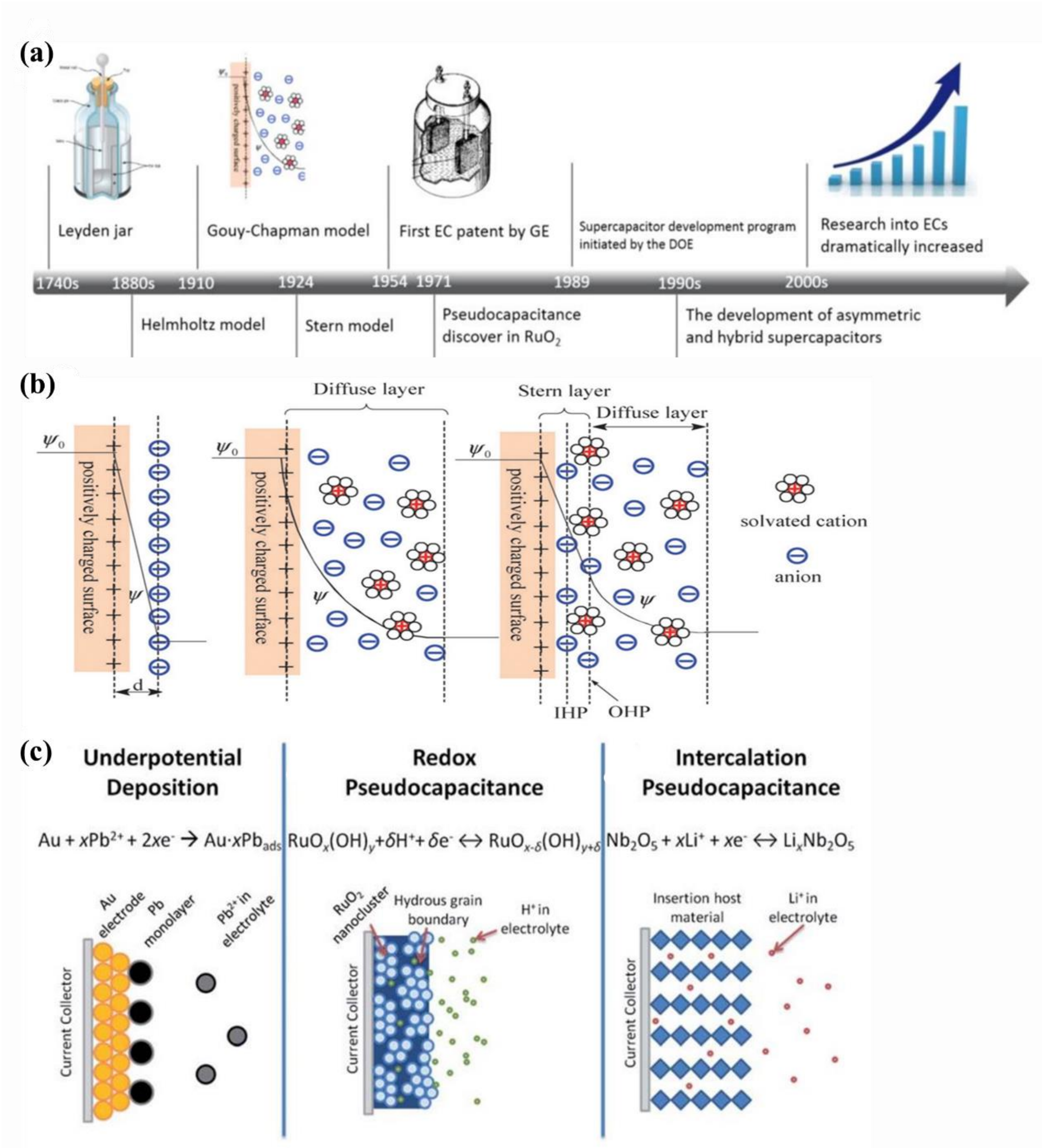

Figure 2: (a) History of SC from Leyden jar until the development of asymmetric and hybrid SC “Adapted with permission [15]. Copyright (2018) American Chemical Society” (b) Gouy-Chapman and Stern model showing IHP and OHP “Adapted with permission [22]. Copyright (2009) Chemical Society Review” (c) pseudocapacitor undergoing the different processes. “Adapted with permission [23]. Copyright (2014), Royal Society of Chemistry”.

Surface redox reaction involves the transfer of electrons between the oxidized and reduced species (redox reactions). The electron transfer rate depends on the electrochemical adsorption of cations. Equation 2 shows the redox reaction:

$$Ox + zC^{+} + Ze^{-} \rightleftharpoons Red\ C_{z} \qquad \text{eq. 2}$$

where C is the electrolyte cation, and Z is the number of transferred electrons [24].

Intercalation and de-intercalation allow the host material to intercalate between the layered electrode and electrolyte interface. This type of behavior allows SC to act as ESS. Equation 3 shows the intercalation and de-intercalation reaction.

$$MA_{y} + xLi^{+} + xe^{-} \rightleftharpoons Li_{x}MA_{y} \qquad \text{eq. 3}$$

where MA_y is the layer-lattice intercalation, and x is transferred electrons [25].

1.4 Basics of water splitting

The chemical reaction through which water splits into hydrogen (H_2) and oxygen (O_2) gas is referred to as water splitting [26]. The evolved H_2 serves as fuel for fuel cells, rockets and can be compressed as a cryogenic liquid which can be later transported for use in different industries. The produced O_2 can be released into the environment or can be stored in liquid form for medicinal purposes. The production of O_2 helps us to face critical situations like COVID [27]. From history to date, there are three ways through which H_2O can be split: steam methane reaction (SMR), coal gasification, and electrolysis of water.

Steam methane reaction occurs during the reaction between natural gas and water [28]. In this reaction, natural gas refers to hydrocarbon methane (CH_4), whereas H_2O is used in steam form, with the very first byproducts being carbon monoxide (CO) and H_2

gas. After this step, reforming occurs, where CO is converted into CO_2 and additional H_2, as shown in **Figure 3(a)**. Equation 4 represents the SMR process.

$$CH_4(g) + H_2O\ (g) \rightleftharpoons 3H_2(g) + CO(g) \qquad \text{eq. 4(a)}$$

$$CO(g) + H_2O(g) \rightleftharpoons CO_2(g) + H_2(g) \qquad \text{eq. 4(b)}$$

This process is endothermic and requires additional heat, so this reaction takes place at a very high temperature (between 700 to 1000 ℃) [29].

Coal gasification is the process of thermochemical conversion of coal or biomass to produce CO and H_2 gas, along with CO_2, and CH_4 [30]. This process can occur in underground mines, and the resulting gases are collected at the surface, as shown in **Figure 3(b)**. Equation 5 shows the coal gasification process [31].

$$3C(s) + O_2(g) + H_2O(g) \rightleftharpoons 3CO(g) + H_2(g) \qquad \text{eq. 5(a)}$$

$$CO(g) + H_2O(g) \rightleftharpoons CO_2(g) + H_2(g) \qquad \text{eq. 5(b)}$$

Electrolysis of water occurs when electricity is passed through H_2O to break it down into H_2 and O_2 [32]. This reaction, which occurs at the anode and cathode of electrodes, is shown in equation 6. The basic schematic of the electrolysis process is shown in **Figure 3c**.

$$H_2O(l) \rightleftharpoons 1/2O_2(g) + 2H^+(aq.) + 2e^-\ \text{(Anode)} \qquad \text{eq. 6(a)}$$

$$2H^+(aq.) + 2e^- \rightleftharpoons H_2(g)\ \text{(Cathode)} \qquad \text{eq. 6(b)}$$

$$H_2O(l) \rightleftharpoons H_2(g) + 1/2O_2(g)\ \text{(Overall process)} \qquad \text{eq. 6(c)}$$

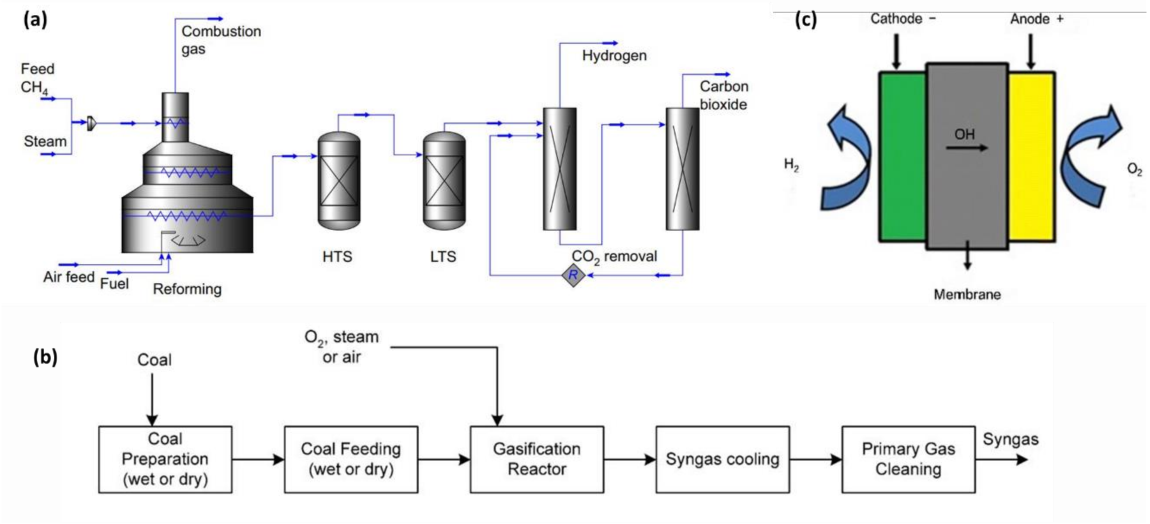

Figure 3: (a) Schematic of SMR "Adapted with permission [28]. Copyright (2015) Elsevier" (b) complete process of coal gasification "Adapted with permission [30]. Copyright (2014) American Chemical Society and (c) basic setup of water electrolysis. "Adapted with permission [33]. Copyright (2018) Springer".

Electrolysis of water can occur through different mechanisms: anion-exchange membrane water electrolysis (AEM), proton-exchange membrane water electrolysis (PEM), and traditional water electrolysis in aqueous solution [34].

Still in its developing phase, anion-exchange membrane water electrolysis is one of the low-cost electrolysis techniques. This process requires an exchange membrane that allows only anions to migrate through its surface. During this process, H_2O is dissociated into H_2 and OH^- ions at the cathode, from where these OH^- ions move towards the anode to produce O_2 gas as shown in **Figure 4(a)**. The reactions taking place during AEM are given in equation 7 [35]:

$$2H_2O(l) + 2e^- \rightleftharpoons 2OH^-(aq.) + H_2(g) \quad \text{(Cathode)} \qquad \text{eq. 7(a)}$$

$2OH^-(aq.) \rightleftharpoons H_2O(l) + 1/2\ O_2(g) + 2e^-$ (Anode) eq. 7(b)

$H_2O(l) \rightleftharpoons H_2(g) + 1/2O_2(g)$ (Overall) eq. 7(c)

AEM still faces some challenges at the industrial level, particularly membrane durability at a low current density.

Proton exchange membrane water electrolysis results in the purest form of H_2 gas, along with environmental cleanliness and better safety. **Figure 4(b)** depicts the PEM process. The membranes used in this process are solid electrolytes, generally made of polymers sandwiched between catalyst layers, allowing H^+ ions to transport through it, producing H_2 gas at the cathode. The reactions taking place during PEM are shown below in equation 8 [36]:

$2H^+(aq.) + 2e^- \rightleftharpoons H_2(g)$ (Cathode) eq. 8(a)

$H_2O(l) \rightleftharpoons 2H^+(aq.) + 1/2O_2(g) + 2e^-$ (Anode) eq. 8(b)

$H_2O(l) \rightleftharpoons H_2(g) + 1/2O_2(g)$ (Overall) eq. 8(c)

Temperature irregularities arising during PEM affect all the parameters of water electrolysis, which further requires a water management system, resulting in higher application cost.

In traditional water electrolysis, which occurs in an aqueous electrolyte solution, hydrogen is evolved at the cathode; this process is referred to as a hydrogen evolution reaction (HER). At the same time, O_2 gas is produced at the anode, called the oxygen evolution reaction (OER). These processes are shown in **Figure 4(c)**.

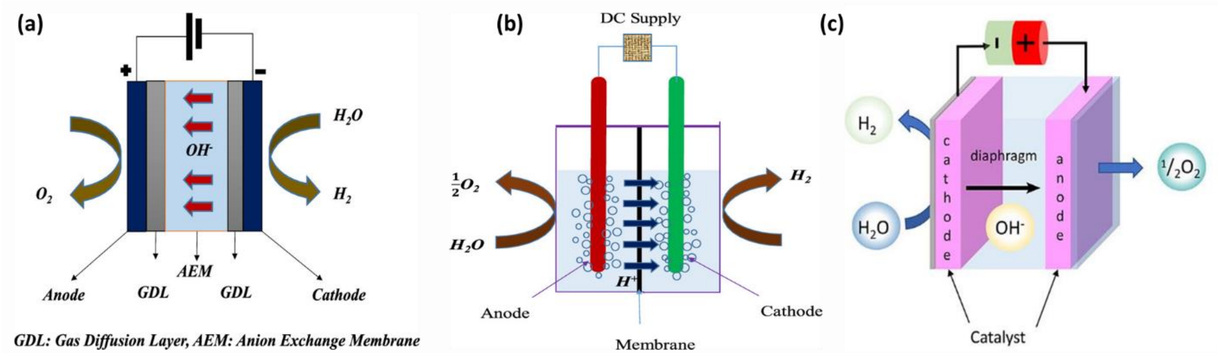

Figure 4: Schematic diagram of water electrolysis via (a) AEM; (b) PEM "Adapted with permission [36]. Copyright (2022), American Chemical Society" and (c) traditional water electrolysis "Adapted with permission [37], copyright (2023) American Chemical Society under common creative attribution 4.0 license permitting it for use in non-commercial aspects".

Traditional water electrolysis is the route to net zero carbon emission. This process occurs in two types of aqueous solutions: acidic and alkaline or neutral. Acidic OER takes place in acidic media, where it again depends on two mechanisms: adsorbate evolution mechanism (Ad. EM), and lattice oxygen evolution reaction (LOER). Ad. EM is the process where H_2O molecules are adsorbed on the catalyst surface, followed by proton-charge transfer, formation of bonds, and adsorption/desorption of surface oxygen to the O_2 molecule. Equation 9 illustrates Ad. EM [38]. Here * refers to the active site.

$H_2O(l) + * \rightleftharpoons H^+(aq.) + HO^*(aq.) + e^-$ eq. 9(a)

$HO^*(aq.) \rightleftharpoons H^+(aq.) + O^*(g) + e^-$ eq. 9(b)

$O^*(g) + H_2O(l) \rightleftharpoons H^+(aq.) + HOO^*(aq.) + e^-$ eq. 9(c)

$HOO^*(aq.) \rightleftharpoons H^+(aq.) + O_2(g) + e^- + *$ eq. 9(d)

$2H_2O(l) \rightleftharpoons 4H^+(aq.) + O_2(g) + 4e^-$ (Overall) eq. 9(e)

The LOER reaction is pH-independent, whereas some processes of OER directly depend on the pH of RHE. In this reaction, the oxygen directly converts to O_2. The primary pathway for the LOER mechanism, given below, is the reaction of lattice oxygen with surface oxygen vacancies (V_o). Equation 10 shows the LOER process [39]:

$OH*(aq.) \rightleftharpoons (V_o + OO^*)(aq.) + H^+(aq.) + e^-$ eq. 10(a)

$H_2O(l) + (V_o + OO^*)(aq.) \rightleftharpoons O_2(g) + (V_o + OH^*)(aq.) + H^+(aq.) + e^-$ eq. 10(b)

$(V_o + OH^*)(aq.) + H_2O(l) \rightleftharpoons (HO\text{-}site^* + OO^*)(aq.) + H^+(aq.) + e^-$ eq. 10(c)

$(HO\text{-}site^* + OO^*)(aq.) \rightleftharpoons OH^*(aq.) + H^+(aq.) + e^-$ eq. 10(d)

Acidic HER is a surface-sensitive reaction and completely depends on the catalyst surface. The major HER activity is related to hydrogen adsorption (H_{ad}) and is determined through Volmer/Heyrovsky or Volmer/Tafel steps, as shown below in equation 11:

$H^+(aq.) + e^- \rightleftharpoons H_{ad}(aq.)$ (Volmer step) eq. 11(a)

$H^+(aq.) + e^- + H_{ad}(aq.) \rightleftharpoons H_2(g)$ (Heyrovsky step) eq. 11(b)

$2H_{ad}(aq.) \rightleftharpoons H_2(g)$ (Tafel Step) eq. 11(c)

Alkaline OER, which takes place on the active site (M), follows exactly the same reaction mechanism as acidic OER, which takes place on the anode [40].

Alkaline HER is the vital process for trading adsorbed hydrogen (H_{ad}), and hydroxyl adsorption (OH_{ad}). It also follows the Heyrovsky and Volmer step, shown below in equation 12. In addition, it includes the water adsorption on the active site, H_2 binding energy, OH^- adsorption strength, and H_2O dissociation ability [41].

$H_2O(l) + e^- \rightleftharpoons OH^-(aq.) + H_{ad}(aq.)$ (Volmer Step) eq. 12(a)

$H_2O(l) + e^- + H_{ad}(aq.) \rightleftharpoons OH^-(aq.) + H_2(g)$ (Heyrovsky Step) eq. 12(b)

Traditional water electrolysis involves an electrocatalyst in an alkaline solution. Theoretically, the H_2O breakdown voltage is 1.23 V versus RHE at room temperature, regardless of medium. However, in practice this process requires a higher voltage. This additional voltage required to break down H_2O into H_2 and O_2 is called overpotential. The reduction or minimization of the overpotential for H_2O breakdown is required in order to make traditional water electrolysis practical for industrial application.

1.5 Materials used for ESS

The gap between the research and commercialization of ESSs could be minimized using suitable materials. However, relevant materials in ESS applications must have certain properties like long-life cycle, high round-trip efficiency, low cost and low maintenance cost, sustainability, and recyclability. Moreover, candidate materials must have potential chemistries applicable to ESS. There are a variety of materials used by researchers, among which carbon, MXene, transition metal hydroxide (TMH), transition metal oxide (TMO), and MOF-based materials are most promising [42].

Carbon-based materials can function as electrode materials because of their porous nature, and the activation of carbon materials enhances their surface area and electrical properties. An advantage of carbon based materials is that the charge accumulation on the surface of the electrode-electrolyte interface results in extraordinary performance. Moreover, the porous carbon-based material exhibit high performance when combined with various types of metallic oxide, hydroxide and 2D layered double hydroxide, and MXenes.

MXenes refer to a class of 2D materials exhibiting high surface area and conductivity. They are synthesized using carbides/nitrates through the MAX phase. Zhon et al. [43] Synthesized $Ti_3C_2T_x$ nanosheets with rGO through the wet spinning method, which exhibits 542 F/cm^3 at a current density of 0.25 A/cm^3. This shows MXene based material is promising for flexible energy devices like medical equipment. However, a better theoretical understanding of MXene is needed to improve the synthesis strategy.

TMH and TMO belong to the class of 2D materials with a layered structure. The majority exhibit valence states that promote electro-sorption or redox reactions leading to high theoretical capacitance and power density. TMO and TMH are comparatively more stable than carbon and MXene-based materials, and they have lower cost [44]. Zhang et al. [45] prepared $Ni(OH)_2$ on mesoporous carbon. This hierarchical structure has a high specific surface area, allowing it to show a high C_{sp} of 2570 F/g at 5 mA/cm^2. Due to the low mass diffusion of hydroxide-based materials, they show sluggish kinetics for the reaction mechanism. However, TMO-based materials have been used for improved electrochemical performance as they exhibit differences in the microstructure. Yi et al. [46] prepared additive-free electrodes of NiO/MnO_2 on nickel foam. As prepared, TMO shows a 3D spherical core-shell structure and improved reaction kinetics in electrolytic solution via ionic diffusion, and it shows a high C_{sp} of 1219 F/g at 20 A/g. Furthermore, the electrochemical properties of these compounds are improved through a specific configuration referred to as MOF, which further increases the active sites and transfer efficiency for charge carriers.

1.6 Metal organic framework

One of the essential factors in improving the performance of ESS is the production of porous materials. MOFs, also called porous coordination polymers (PCP), are crystalline materials with high porosity. MOFs generally have a cage-like structure with connections, referred to as coordination chemistry. The first review of the Prussian Blue complex around 1964 shows interest in PCPs. Moreover, during the 1990’s the seminal catalysis work by Hoskins and Robins created the platform for MOFs. In 1995, Yaghi et al. [47,48] popularized the term MOF using a layered co-structure with reversible sorption. The fundamental structure of a MOF is a center point consisting of metal and linkers (ligands) provided by the organic structure. The metal and organic components act synergistically, enhancing the performance of their precursor materials and providing stability. MOFs have advantages over other materials due to their tunable porosity and structure. Various factors like the synthesis route, precursors used, temperature, and particle size can affect the performance of MOF-based materials. MOFs have been used for multiple applications as shown in **Figure 5** [49]. Nanostructured-based MOF materials have the potential for a larger number of active sites for transferring electrons and ions with high mass deposition, allowing its primary application in ESS.

Lin et al. [50] synthesized a MOF-based structure of CO_3O_4 and ZnO on a carbon electrode where they found the structure of MOF to be a core-shell type of structure. It was tested in 6M KOH electrolytic solution, where it exhibited 43 Wh/kg and 1402 W/kg of energy and power density. Moreover, to understand the synergism of the combination of two different MOFs, Lang et al. [51] fabricated MOF of Ni/Co/Fe using a solvothermal synthesis route. The cage-like structure allowed excellent OER performance with an active metallic core and higher binding energy, lowering the overpotential to 219 mV at 10 mA/cm^2. Also, the bulk 3D structure provided a faster kinetic reaction.

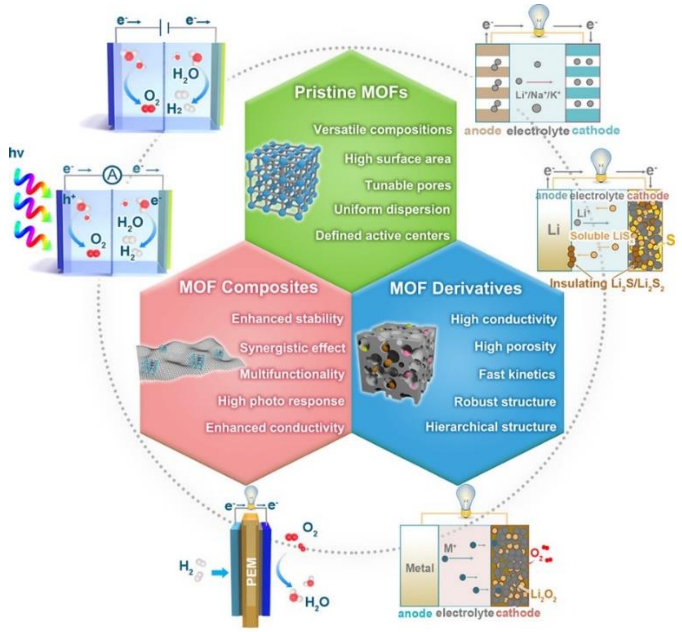

Figure 5: Merits and applications of MOFs. "Adapted with permission [52]. Copyright (2020), American Chemical Society".

1.7 Objective of the thesis

MOF-based materials are widely utilized as bi-functional materials in energy conversion and storage devices due to their plentiful active sites and easily tunable properties. In this research, a simple hydrothermal method was used to synthesize NH and NO-MOFs to obtain MOF-based materials with numerous active sites. Also, to optimize the performance of these MOFs, the synthesis temperature was varied accordingly. The synthesis of MOFs was confirmed using various characterizations like XRD, FT-IR, and SEM. These MOF-based materials then served as the electrode materials for application in SC and as electrocatalysts.

CHAPTER II

EXPERIMENTAL DETAILS

2.1 Synthesis of metal hydroxide and metal-oxide MOF

2.1.1 Materials

Nickel acetate [$Ni(CH_3COO)_2.4H_2O$] was purchased from Acros Organics. Glutaric acid ($C_5H_8O_4$) was purchased from TCI, America. Potassium hydroxide (KOH), ethanol (C_2H_5OH), D.I. H_2O, and sodium hydroxide (NaOH) were purchased from Fisher Scientific, USA. Nickel foam activated carbon (AC), n-methyl-polypyridine (NMP), and polyvinyl-di fluoride (PDVF) were purchased from MTI Corporation, USA.

2.1.2 Synthesis of nickel hydroxide MOF (140, 160, and 180 ℃)

NH-based-MOF was synthesized using 3 mmol $Ni(CH_3COO)_2.4H_2O$ as an inorganic precursor with 3 mmol $C_5H_8O_4$ as an organic ligand to form the cage-like (rod-like) structure for the development of the framework. In addition, 0.2292 gm of KOH was used to maintain the neutrality of the solution with an acidic ligand. A 1:1 mixture of 20 mL distilled H_2O and C_2H_5OH was used as the solvent. To keep the solution's pH to ten, 2 mL of NaOH (0.4 M) aqueous solution was added to the above solution under sonication for 10 min. Subsequently, the prepared solution was transferred to the Teflon-lined autoclave (45 mL) at 160 ℃ for 24 h. The solution was cooled to room temperature after the reaction. Finally, the obtained solution was washed several times with distilled H_2O

and C_2H_5OH and centrifuged for 10 min. The obtained NH-MOF-160 was dried overnight at 70 °C in the oven and ground using a hand mortar and pestle to very fine powder of pale green color. The same process was used for NH-MOF at 140 and 180 °C.

2.1.3 Synthesis of nickel oxide MOF (140, 160, and 180 °C)

The obtained NH-MOF (160 °C) was calcined at 350 °C for 2 h in a muffle furnace where NH-MOF-160 °C was converted to NO-MOF-160 °C with black powdered color. The same process is used for NO-MOF (140 and 160 °C).

2.1.4 Preparation of electrodes

The working electrodes were prepared by mixing 80 wt.% synthesized materials, 10 wt.% PVDF (binder), and 10 wt.% activated carbon (conductive additive) in the presence of NMP solvent. The Ni foam (substrate) was dipped into the paste and dried at 70 °C for 48 h. The mass loading on all the electrodes varies between 2 to 3 mg.

2.2 Devices used for structural characterization

2.2.1 X-ray diffraction

X-ray diffraction consists of two primary terms: X-ray, produced through a cathode ray tube, and diffraction phenomena, which refers to the modification or spreading of a light ray when passed by the edges of an opaque body or narrow opening. This technique is used to study the type of crystal structure and atomic spacing between the crystal lattice planes. It works on the diffraction principle, which is explained by Bragg's equation: $2d \sin\theta = n \lambda$, where n is the integer, λ is the wavelength of incident X-ray, θ is the diffraction angle, and d is the interplanar spacing between two adjacent planes [53]. In this study, copper Cu ($K_\alpha = 1.5418$ Å) was used as X-rays. The intensities of these x-rays after bombardment on the sample over a range of 2θ ($10^o \leq 2\theta \leq 80^o$) was recorded through an

X-ray detector. A Shimadzu X-ray diffractometer of Lab-X-6100 (shown in **Figure 6)** was used in this research.

Figure 6: Left image shows the front view of XRD instrument and right image shows the source, detector, and sample holder.

2.2.2 Scanning electron microscope

SEM was used to study the surface topography of the as-prepared MOFs at a magnified scale. The operation of the SEM depends on the scattering of electrons obtained after striking the surface of the specimen. These scattered electrons are of different types, including X-ray electrons, which provide information about composition; auger electrons, which further identify the surface sensitivity; cathodoluminescence, which also provides information about electrical sensitivity; backscattered electrons, which deal with the topographical and atomic number information; and secondary electrons, which relate the complete information of topographical structure. The SEM is made up of an electron optical system, specimen stage, secondary electron detector, operating system, and image display unit [54]. The SEM device used in this work was HITACHI SU-5000 (shown in **Figure 7**).

Figure 7: Image of SEM instrument.

2.2.3 Energy dispersive spectroscopy

The SEM was also used to perform energy dispersive spectroscopy to determine the uniform distribution and elemental composition of samples. This technique works on the capacity of high energy electromagnetic radiation (X-rays) to eject core electrons from an atom. According to Moseley’s law, the atomic number of an atom is directly correlated to the frequency of light released when core electrons are ejected. The specimen further exhibits the X-ray peaks from the ground and higher transition shells in combination with bremsstrahlung signals. This signal is converted to a voltage signal through a pulse processor detector which requires a constant time for better spectral resolution [55]. The EDS used in this research is shown in **Figure 8**.

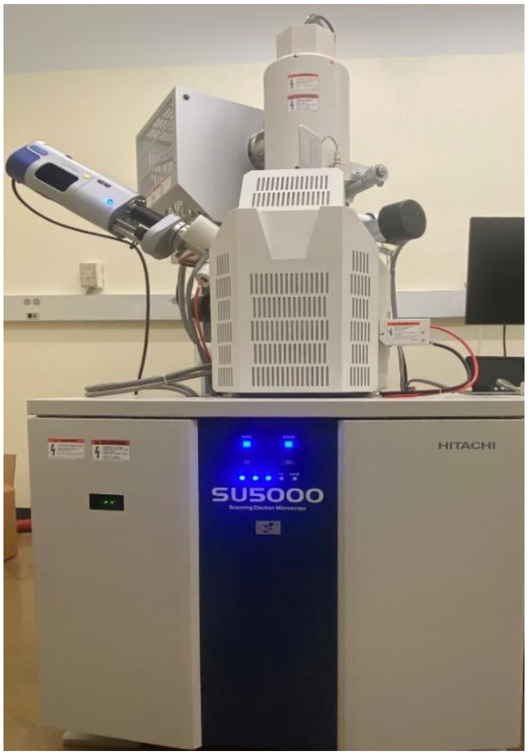

Figure 8: Image of SEM-EDS instrument.

2.2.4 Fourier transform-infrared spectroscopy

Fourier transform-infrared spectroscopy is a technique used to study chemical bonds, chemical compounds, and substituent groups using IR rays. This technique works on the principle of molecular vibrational and rotational motion. This research used a PerkinElmer spectrum two UATR (shown in **Figure 9**), which includes an IR signal production device called an interferometer, sample holder, detector, amplifier, and analog-to-digital converter. The IR signal passed through the sample is amplified using an amplifier and converted to a digital signal using analog to digital converter. This signal is transmitted to the screen as an image after Fourier transformation [56].

Figure 9: Image of FT-IR instrument.

2.3 Electrochemical testing

The electrochemical measurements were carried out with a Versastat 4-500 workstation (Princeton Applied Research, TN, USA) at room temperature using three electrode configurations. To study the electrocatalytic activity, Ag/AgCl (sat. KCl) was used as a reference electrode, while for supercapactive studies, Hg/HgO was used as a reference electrode. For both systems, a platinum wire was used as a counter electrode. 1M and 3M KOH solutions were used as the electrolyte for electrocatalytic and supercapactive studies, respectively. Linear sweep voltammogram (LSV) was recorded at a fixed scan rate of 2 mV/s. All potentials were converted to a reversible hydrogen electrode (RHE) using the following equation $E_{RHE} = E_{Ag/AgCl} + E^{o}_{Ag/AgCl} + 0.059\ pH$. The operating voltage window for SC studies was 0-0.6 V. In the case of SC testing, cyclic voltammetry (CV) and galvanostatic charge-discharge (GCD) measurements were employed. **Figure 10** shows the image of Princeton workstation used in this study.

Figure 10: Image of workstation used for electrochemical testing.

CHAPTER III

RESULTS AND DISCUSSION

3.1 Structural characterization

3.1.1 X-ray diffraction

The XRD of all the as-prepared MOFs was carried out in the range of 2θ = 10 to 80º. **Figure 11(a)** shows the XRD peaks of all NH-MOFs corresponding to 2θ = 13.94, 16, 24.06, 29.06, 31.66, 33.88, 34.78, and 60º, which confirms the planes (010), (101), (006), (002), (020), (111), (012), and (110), respectively [57]. The peaks of these MOFs corresponds to the mixed phases (α and β) of $Ni(OH)_2$-based MOF. The crystallinity of each MOF was calculated using equation 13, from which it is found that the crystallinity of MOFs increases with the increase in the temperature at which it was produced [58]. The NH-MOF-180 shows the highest crystallinity of 78.35%. **Figure 11(b)** shows the XRD pattern of NO-MOFs, where 2θ = 37.46, 44.7, 63.14, 75.52, and 77.2º (represented by [*]) with (111), (200), (220), (311), and (222) planes of NiO-based MOFs. The peaks at 43.46 and 52º correspond to the Ni_2O_3 reduced from NiO during combustion at higher temperature, with crystal planes (111), and (200) (represented by [$]) [59]. The NO-MOF-180 exhibits the highest crystallinity of 79.09%.

$$Crystallinity\ \% = \frac{Area\ of\ Crystalline\ peaks * 100}{Area\ of\ all\ peaks} \qquad eq. 13$$

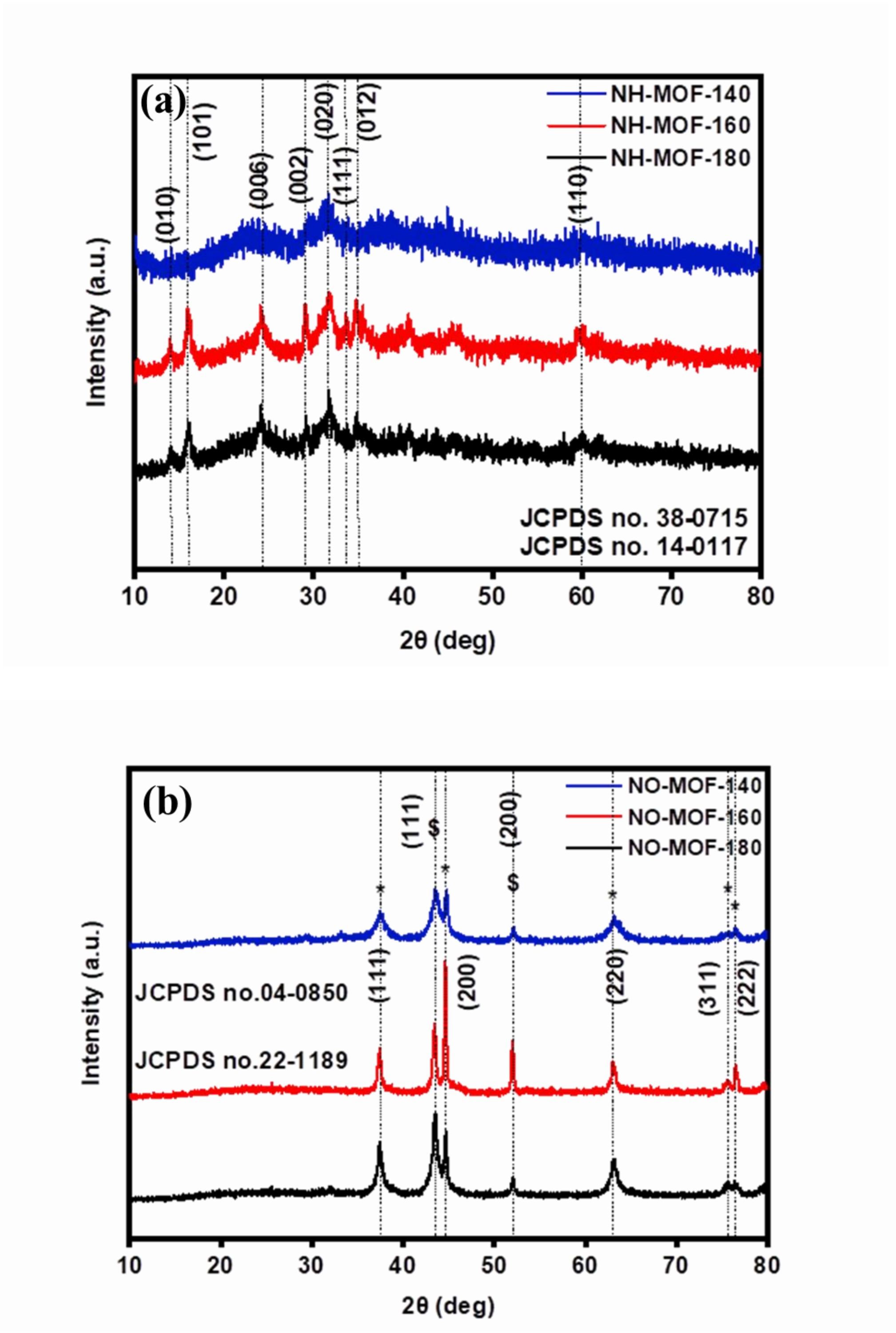

Figure 11: XRD pattern of (a) NH-MOF; and (b) NO-MOF based samples.

3.1.2 Fourier infrared transform spectroscopy

FT-IR confirms the presence of functional groups. In **Figure 12(a)**, the peak at 2974 cm^{-1} corresponds to stretching vibration of C-H bonds, while the peaks at 1576 and 1483 cm^{-1} correspond to C=C and stretching vibration of -COOH. The peak at 648 cm^{-1} arises from the in-plane Ni-OH bending vibration of α-$Ni(OH)_2$ lattice [60]. In **Figure 12(b)**, the peak at 1344 cm^{-1} is due to the presence of C-O stretching vibration. The peak at 648 cm^{-1} corresponds to the strong vibration of Ni-O bonds [61].

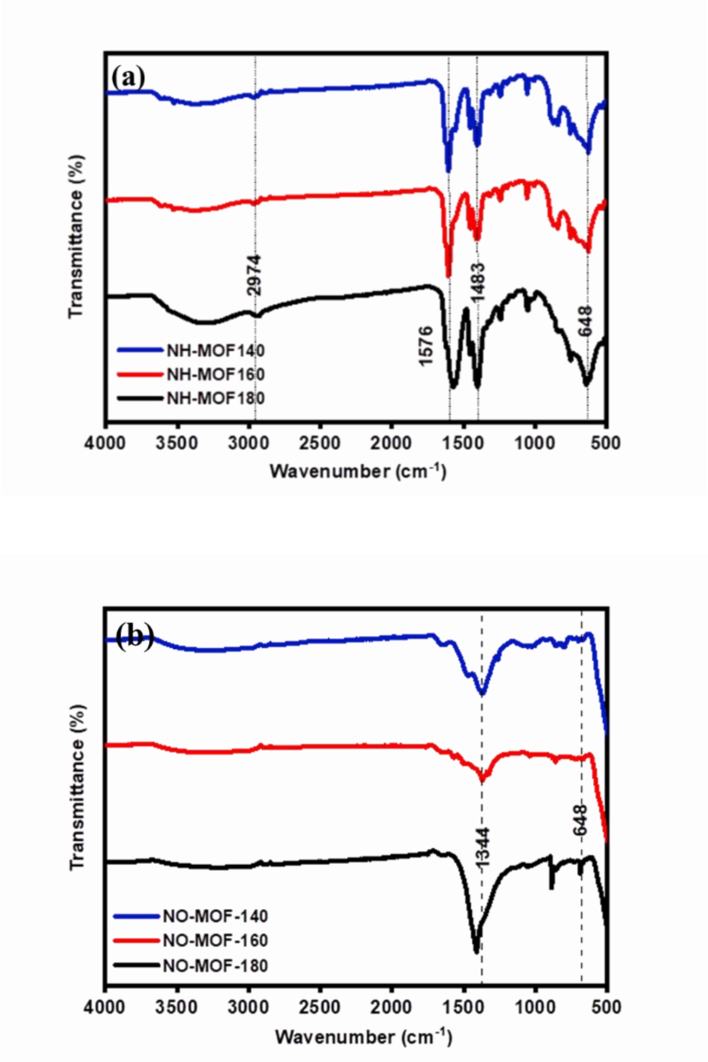

Figure 12: FT-IR pattern of (a) NH-MOF; and (b) NO-MOF based samples.

3.1.3 Scanning electron microscopy

The SEM was deployed using high (50 µm) and low (100 µm) resolution to study the morphology of as-prepared MOFs. At low resolution, the morphology of NH-MOF-140 appears to be agglomerated particles; at high resolution, agglomerated particles attached to the surface of a thick sheet were observed (shown in **Figure 13(a-b)**). At low resolution, the NH-MOF-160 appears to have a flat, rock-like [62] morphology, which is further confirmed at high resolution, where it exhibits small agglomerated rocks attached to a flat surface, as shown in **Figure 13(c-d)**. Increasing the temperature of production of NH-MOF resulted in more agglomeration (**Figure 13(e-f)**). Similarly, at low resolution, NO-MOF-140 exhibited agglomerated [63] particles, which at high resolution appear to be thick, sharp crystallites (**Figure 13(g-h)**). The particles are more agglomerated as the temperature of production increased from 140 to 180 ℃ (**Figure 13(i-l)**).

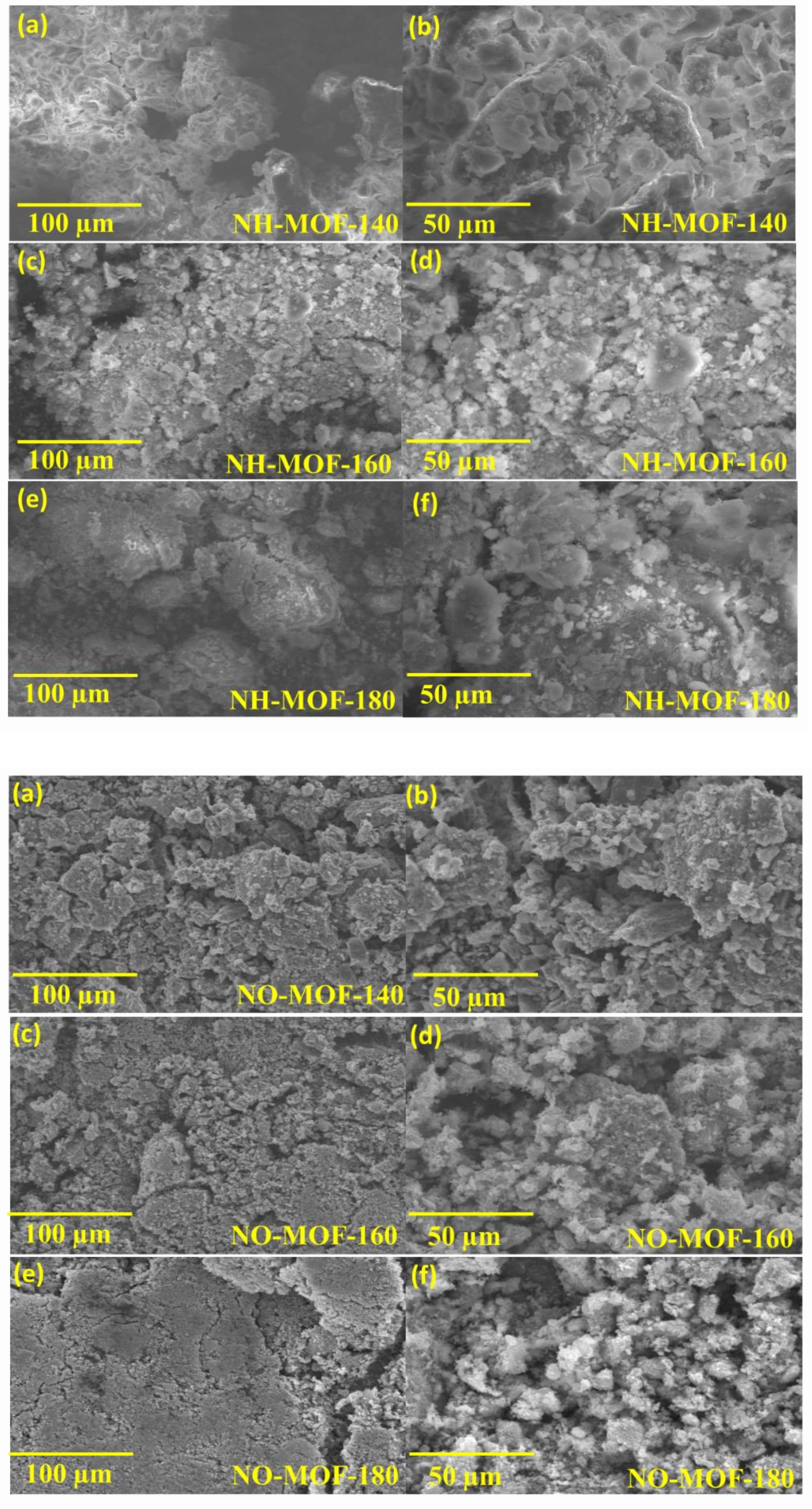

Figure 13: SEM images of NH-MOF; and NO-MOF based samples.

3.1.4 Energy dispersive spectroscopy

Elemental mapping was used to confirm the presence of elements as well as their distribution over the surface of as-prepared MOFs. **Figure 14** confirms the major element Ni, O, and C for NH-MOFs and NO-MOFs. Moreover, the magnified map image show that NH-MOF-160 had the most uniform deposition of Ni, resulting in its better performance when compared to other synthesized MOFs [64].

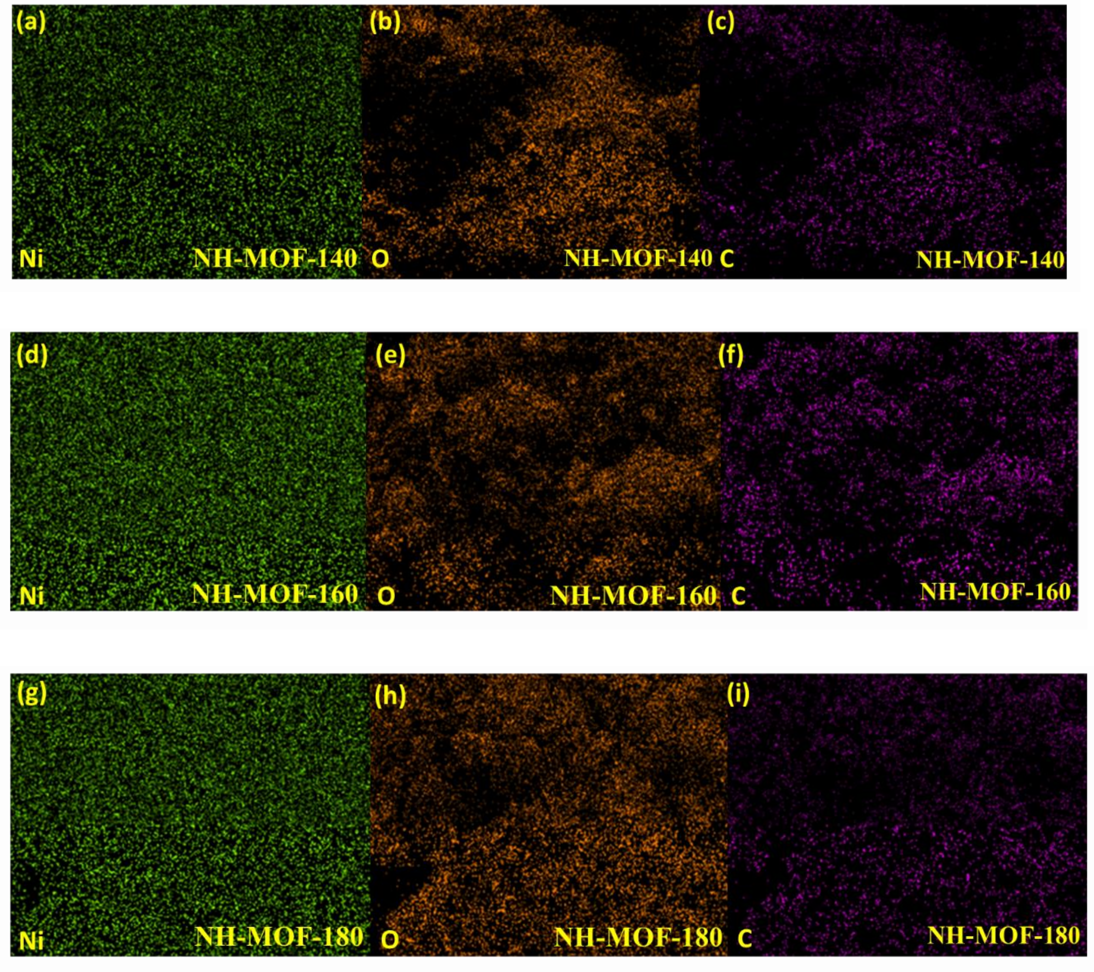

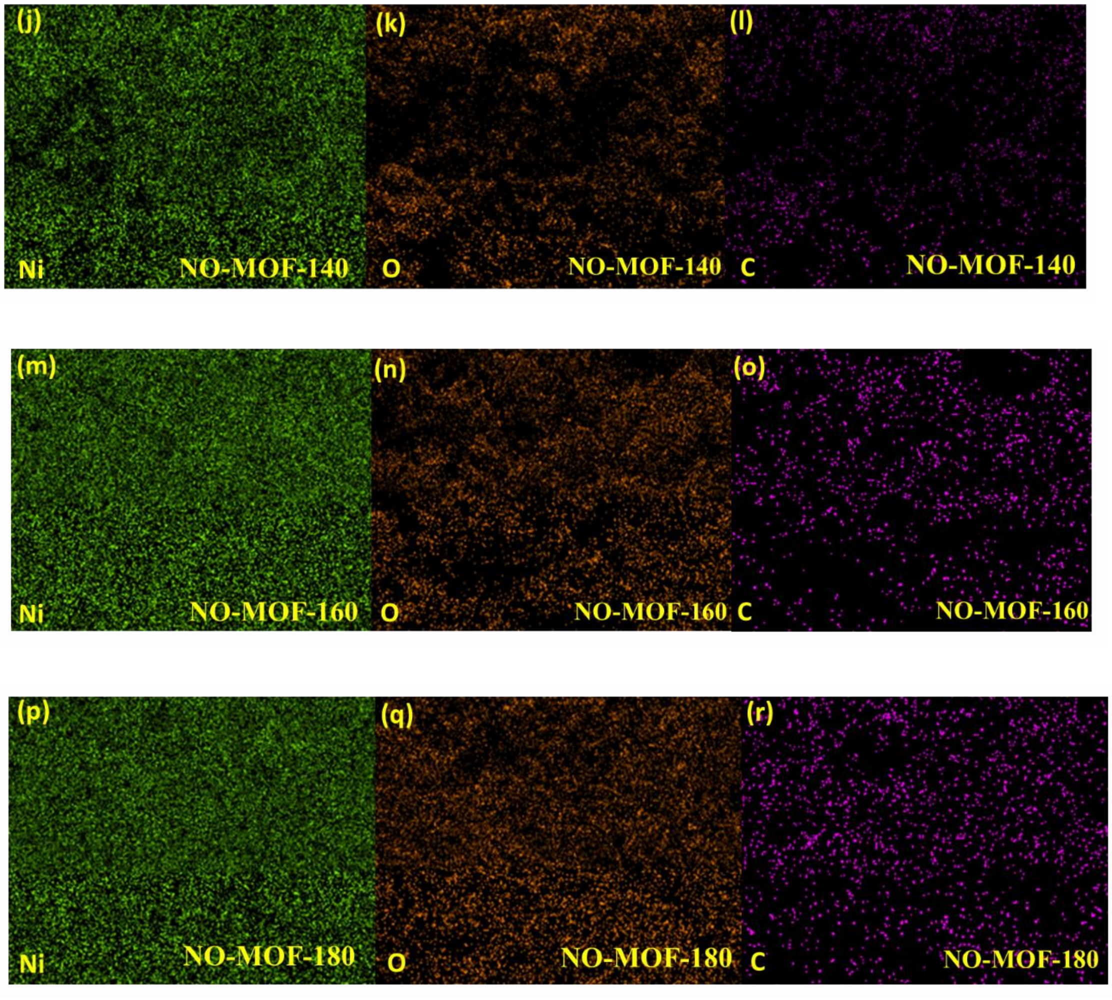

Figure 14: EDS mapping of NH-MOF and NO-MOF based samples.

3.2 Electrochemical measurements

3.2.1 Supercapacitive study

To determine the capacitive performance of as-prepared MOFs, CV curves were produced at various scan rates (2 to 300 mV/sec). All the as-prepared NH-MOFs showed oxidation and reduction peaks in the 0.4 – 0.55 V and 0.28 – 0.34 V ranges; all the NO-MOFs exhibited oxidation and reduction peaks under the range of 0.41 – 0.48 V and 0.3 – 0.35 V as shown in **Figure 15**. All these peaks are attributed to the transfer of electrons through the reaction $Ni^{2+} + 2e^{-} \rightleftharpoons Ni$ [65]. The NH-MOF-160 and NO-MOF-160 exhibited the highest current density, predicting better performance. The faradaic and capacitive controlled processes can be shown using equation 14.

$$i = av^{b} \qquad \text{eq. 14}$$

where *i* is the current density, *v* is the scan rate, *b* is the slope of the plot of log (scan rate), v/s log (current density), and *a* is the intercept on Y-axis [65,66].

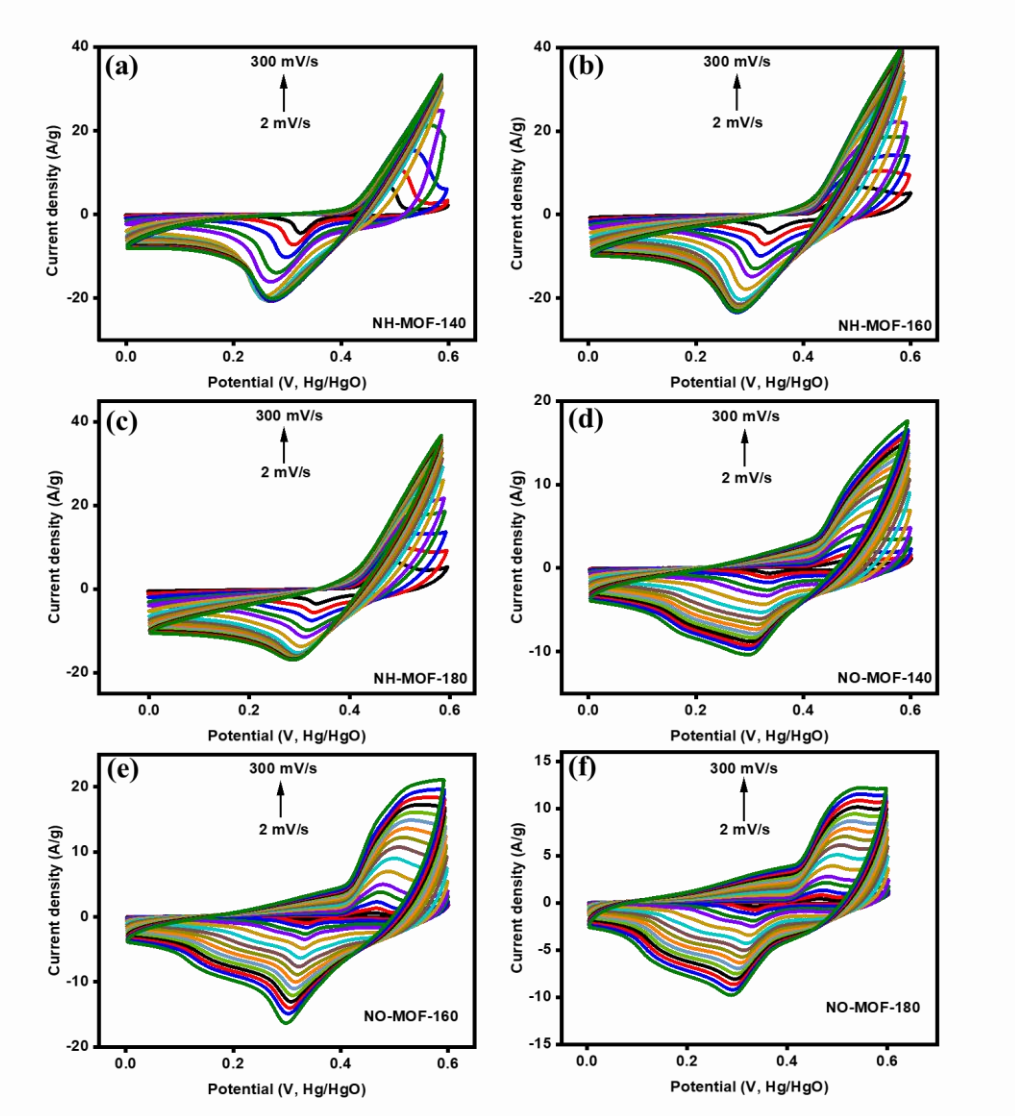

Figure 15: CV curves at various scan rate of NH-MOF and NO-MOF based samples.

If b=1, the SC exhibits a pure capacitive mechanism, whereas if b=0.5, it exhibits diffusion-controlled phenomena. As shown in **Figure 16(a-b)**, all the as-prepared MOFs exhibited a hybrid behavior. The capacitance contribution at various scan rates was calculated using equation 15

$$i = k_1 v + k_2 v^{1/2} \qquad \text{eq. 15}$$

where, $k_1 v$ represents the capacitive behavior, and $k_2 v^{1/2}$ indicates the diffusion effect [67]. **Figure 16(c-d)** shows the diffusion and capacitance contribution at 5 and 50 mV/sec. The NH-MOF-160 exhibits the highest diffusion contribution of 97% at 5 mV/sec; for NO-MOF-160, it was 89% at the same scan rate. The diffusion contribution allows more ions to be oxidized and reduced over the surface of electrodes, providing improved ionic mobility. Increased capacitive properties of MOFs are observed at higher scan rates, as shown in **Figure 16(e-f)**, reducing their charge storage properties.

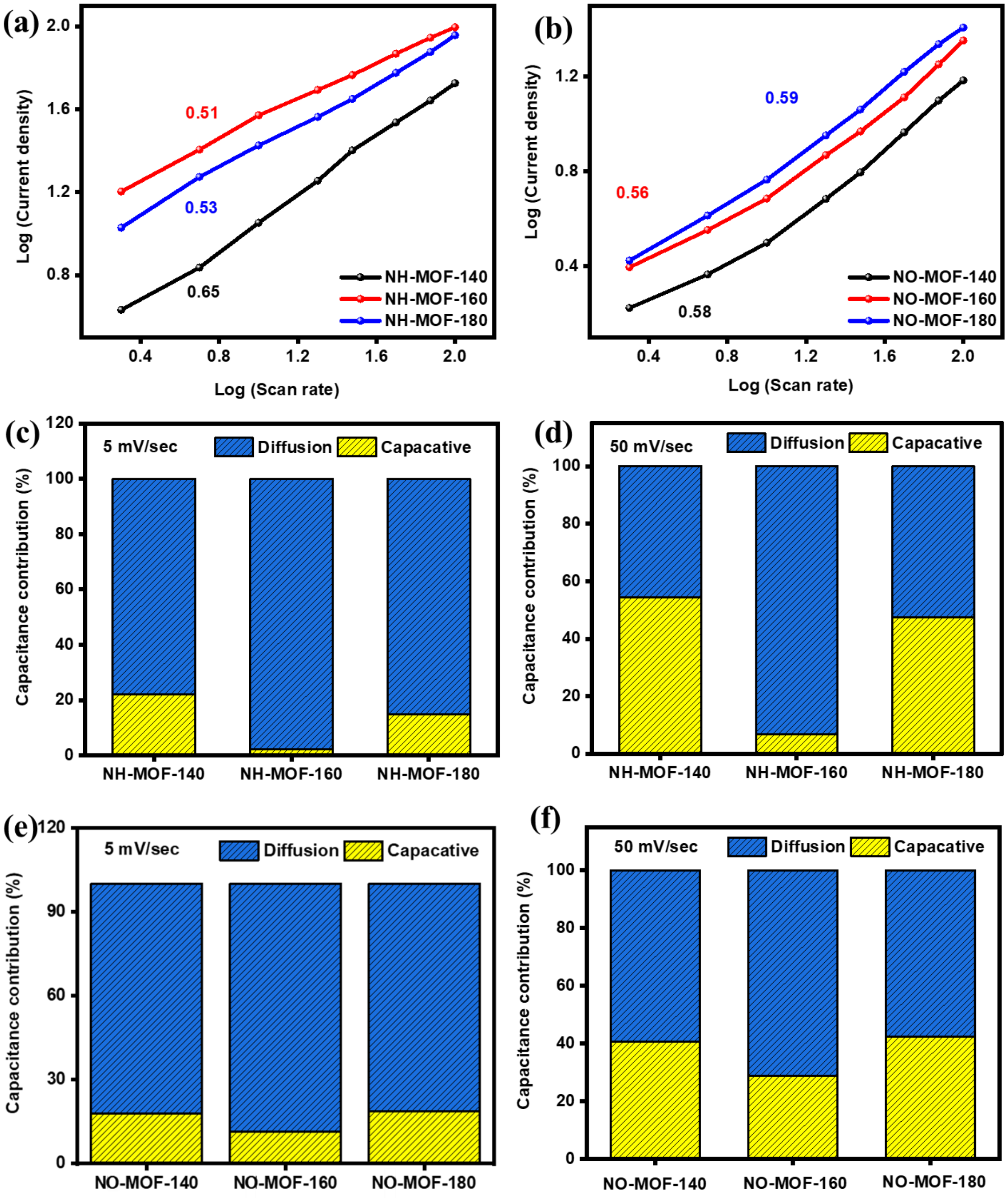

Figure 16: Log (scan rate) v/s log (current density) curves of (a)NH-MOF; (b) NO-MOF; and (c-f) capacitance contribution of NH-MOF; and NO-MOF at 5 and 50 mV/sec scan rates.

The MOFs’ charge storage capacities at various current densities (1 A/g to 30 A/g) are shown in **Figure 17**, which depicts the non-linear behavior of the GCD curves. The non-linear GCD curves are caused by quasireversible faradaic reactions, which leads to non-uniform charge/voltage ratio with respect to time [68].

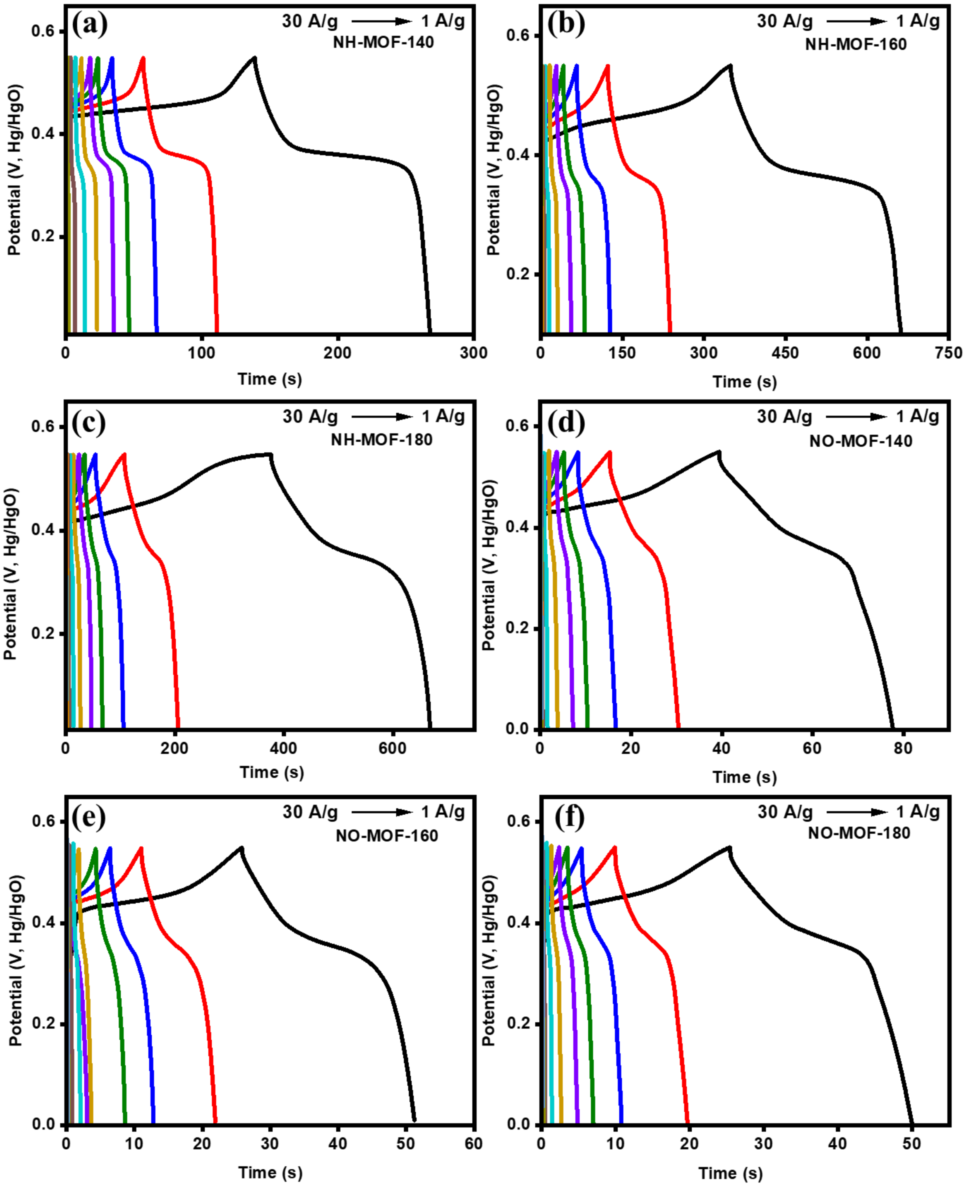

Figure 17: GCD curves of NH-MOF; and NO-MOF based samples.

The MOFs' C_{sp} at different current densities was calculated using equation 16 [69],

$$C_{sp} = \frac{i\Delta t}{m\Delta V} \qquad \text{eq. 16}$$

where i is the current, m is the active mass of the electrode, Δv is the applied potential window, and Δt (sec) is the time taken for complete discharge. The C_{sp} at 1 A/g was highest for NH-MOF-160 (608 F/g), followed by NH-MOF-180 (545 F/g), and NH-MOF-140 (282 F/g). These results also show the effect of temperature of production on the C_{sp} of MOFs. The C_{sp} at 1 A/g for NO-MOF-160 was 78 F/g. The C_{sp} versus current density curves at different scan rates are shown in **Figure 18(a-b)**. The C_{sp} was also calculated using equation 17(a),

$$C_{sp} = \frac{A}{vm\Delta V} \qquad \text{eq. 17(a)}$$

where A is the area under the CV curve, *v* is the scan rate, Δv is the operated potential, and m is the active mass of the electrode. The quantitative analysis of GCD at different current densities was supported through C_{sp} (areal capacitance) versus scan rate curves, where NH-MOF-160 shows a C_{sp} of 1482 F/g at 2 mV/sec. At lower scan rates, a diffusion-controlled mechanism facilitates the higher C_{sp}. In contrast, ions have less time to perform surface redox reactions at a higher scan rate, so they tend to exhibit reduced capacitive energy storage as shown in **Figure 18(c-d)**. All the as-prepared MOFs' energy and power density was calculated using equation 17(b and c),

$$E = \frac{1}{2}C\Delta V^2 \qquad \text{eq. 17(b)}$$

$$P = \frac{E}{\Delta t} \qquad \text{eq. 17(c)}$$

where C is the specific capacitance, Δv is the potential window, and Δt is the discharge time [70]. The Ragone plot for the energy and power density of both MOFs is shown in **Figure 19**.

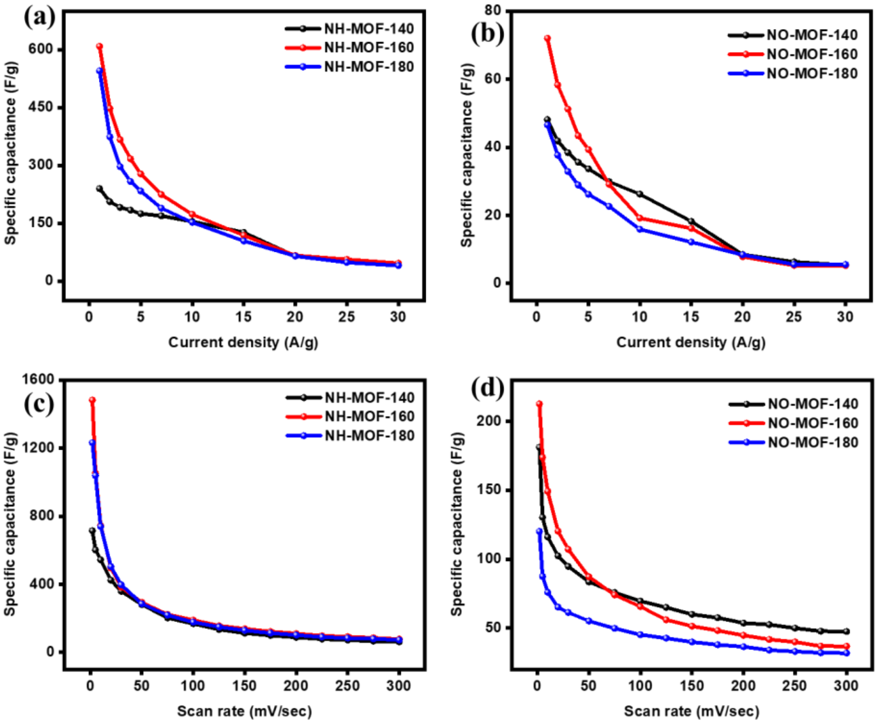

Figure18: (a-b) C_{sp} v/s current densities; (c-d) C_{sp} v/s scan rates of NH-MOF; and NO-MOF based samples.

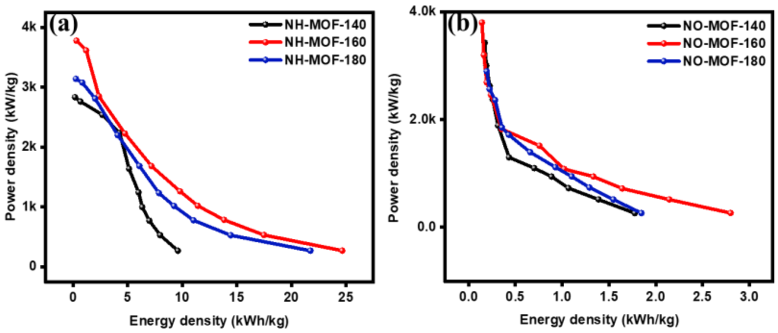

Figure 19: Ragone plot of (a) NH-MOF; and (b) NO-MOF based samples.

The GCD curves at 1 A/g for NH-MOFs and NO-MOFs are shown in **Figure 20**, where NH-MOF-160 requires less time to charge completely and allows itself to discharge slowly. During SEM it was observed that NH-MOF-160 shows a flat surface which provides more area for ions to attach on its surface and offers better charge storage capacity when compared to other prepared MOFs [71]. Compared to other as-prepared MOFs, NO-MOF-160 requires more time to charge and also more time to discharge. The longer time during charging is due to highly agglomerated particles, as observed in SEM images, which further affect its charge storage capacity.

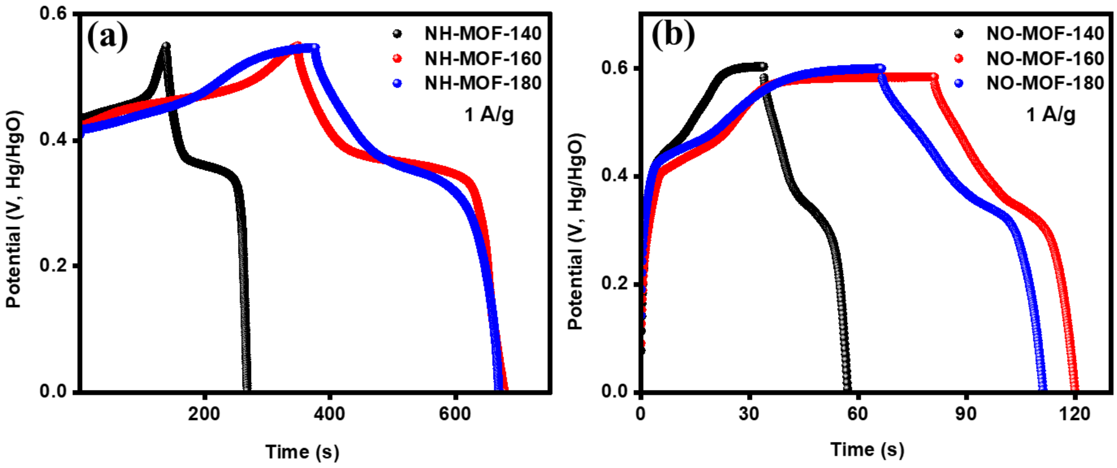

Figure 20: GCD curves of (a) NH-MOF; and (b) NO-MOF based samples at 1 A/g.

Electrochemical impedance spectroscopy (EIS) measurements were carried out to better understand the electrochemical properties of as-prepared MOFs, using Nyquist plots to depict the type of capacitive behavior. The ideal Nyquist plot depicts the semicircular region indicating ideal capacitive behavior, while the vertical line attached to the semicircle exhibits non-ideal behavior. The equivalent series resistance (ESR-R_s-intercept at the x-axis), which is the combination of the ionic resistance of the electrolyte and the interfacial resistance of the active surface of materials, is shown in the Nyquist plots in **Figure 21**. The charge transfer mechanism relates to the charge transfer resistance (R_{ct}) determined through semicircles in the high-frequency region. The NH-MOF-160 showed the lowest possible R_s value of 1.01 Ω, and the NO-MOF-160 showed the lowest R_s value of 0.96 Ω.

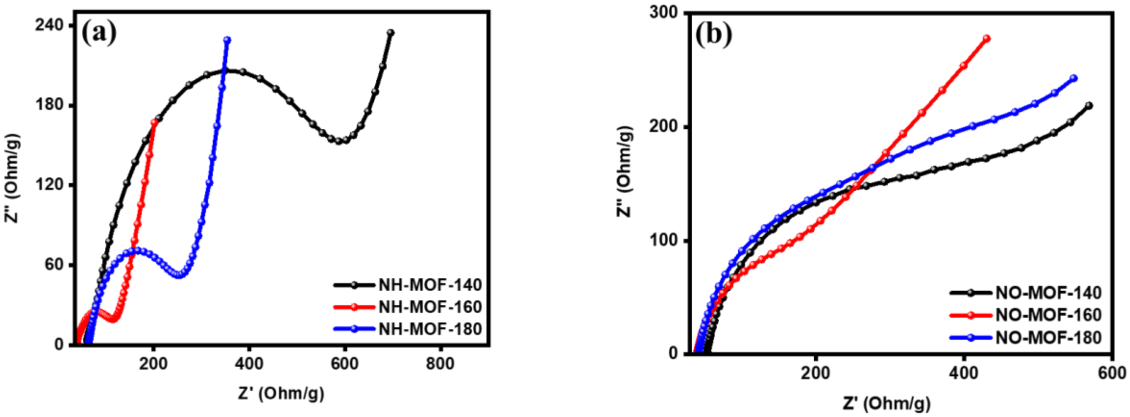

Figure 21: Nyquist plot for (a) NH-MOF; and (b) NO-MOF at 0 V versus Hg/HgO.

The stability of as-prepared MOF electrodes was explored through GCD curves as shown in **Figure 22**. The GCD was carried out for 5000 cycles, and all the electrodes exhibited high stable cycling performance. The NH-MOFs exhibited charge retention of 92, 94, and 90%, whereas the NO-MOFs showed 84, 89, and 87% retention in capacitance. In addition, all the as-prepared MOFs exhibited an average retention of 97% in coulombic efficiency, as shown in **Figure 22**.

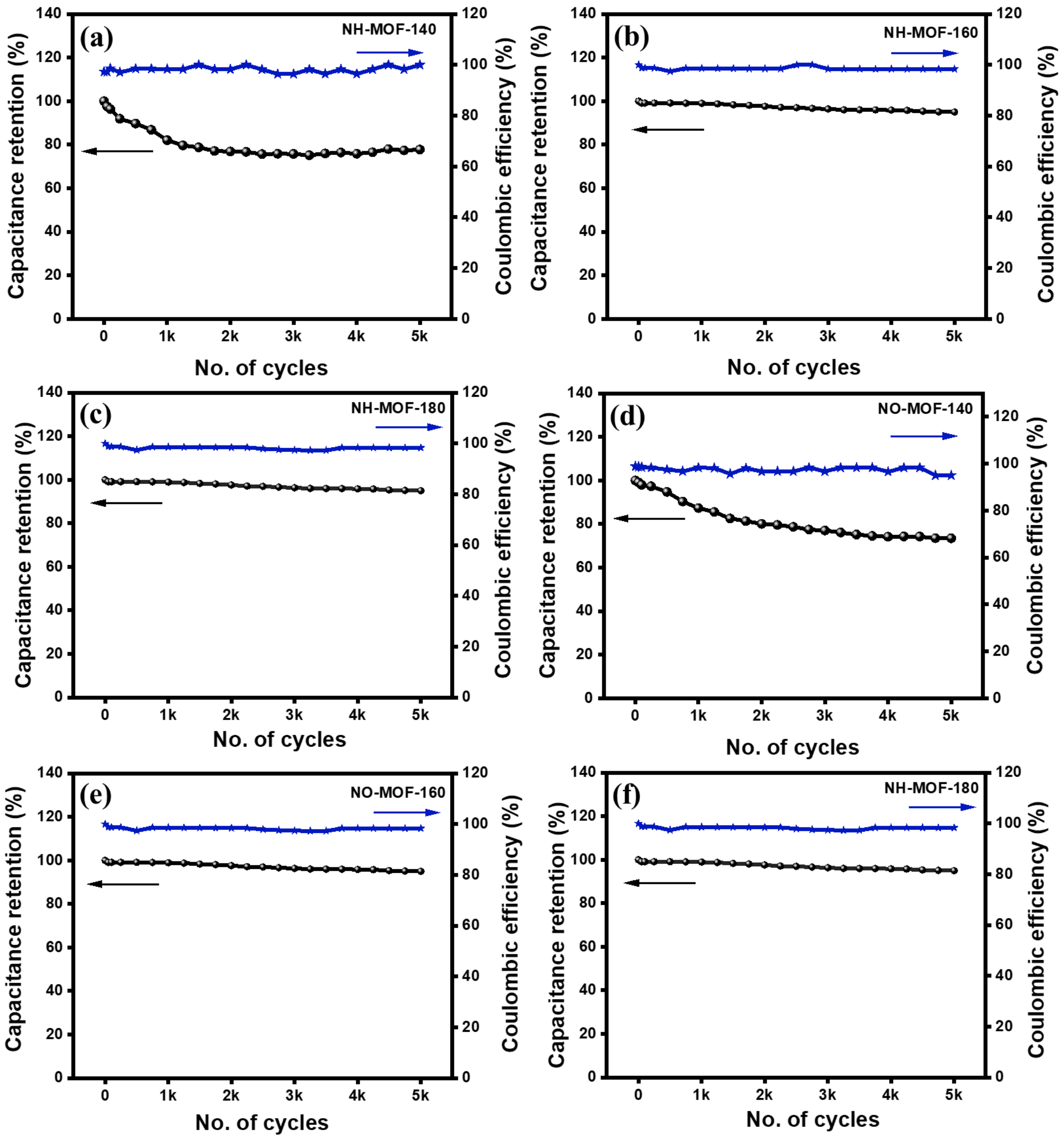

Figure 22: Retention in capacitance and Coulombic efficiency of NH-MOF; and NO-MOF based samples.

Table 1. Comparison between various data of supercapacitor.

Sample name	**Specific capacitance (F/g)**	**Current density**	**References**
Inverted Ni-MOF	533	1	[72]
Flake Ni-MOF	498	1	[73]
Ni/Co-MOF	544	1	[74]
Ni/Co-MOF	523.4	1	[74]
Ni-MOF	503	1	[75]
Ni(OH)(COO)$_6$/GO	590	1	[76]
NH-MOF-160	**608**	**1**	**This work**
NH-MOF-180	**545**	**1**	**This work**

3.2.2 Electrocatalytic water splitting

To determine the catalytic properties of prepared NH and NO-MOFs, HER and OER have been performed. The HER polarization curves for all MOFs are shown in **Figure 23(a-b)**. To reach a current density of 10 mA/cm^2, NH-MOF-160 required 176 mV, while NO-MOF-160 required 217 mV. Furthermore, the performance of all MOFs was affected by the temperature of production. The HER mechanism is explained based on Volmer and Heyrovsky's step in equation 12(a and b). The Volmer step determines the onset potential, which makes it possible to calculate current density. For NO-MOF-160 and NH-MOF-160, current density was found to be 48.5 and 51.6 mA/cm^2, indicating the enhanced water dissociation property of NH-MOF-160. The Heyrovsky step is the rate-limiting electrochemical desorption step, which controls the kinetics of the reaction through the cathodic Tafel slope [77]. The equation 18 was used to calculate the Tafel slope.

$$\eta = \mathrm{a} + \mathrm{b}\log j \qquad \text{eq. 18}$$

where η corresponds to overpotential, j is the current density, a is the intercept at Y-axis, and b represents the Tafel slope [78]. NH-MOF-160 and NO-MOF-160 exhibited 116 and 127 mV/dec respectively, indicating the faster rates of NH-MOF-160, as shown in **Figure 23(c-d)**.

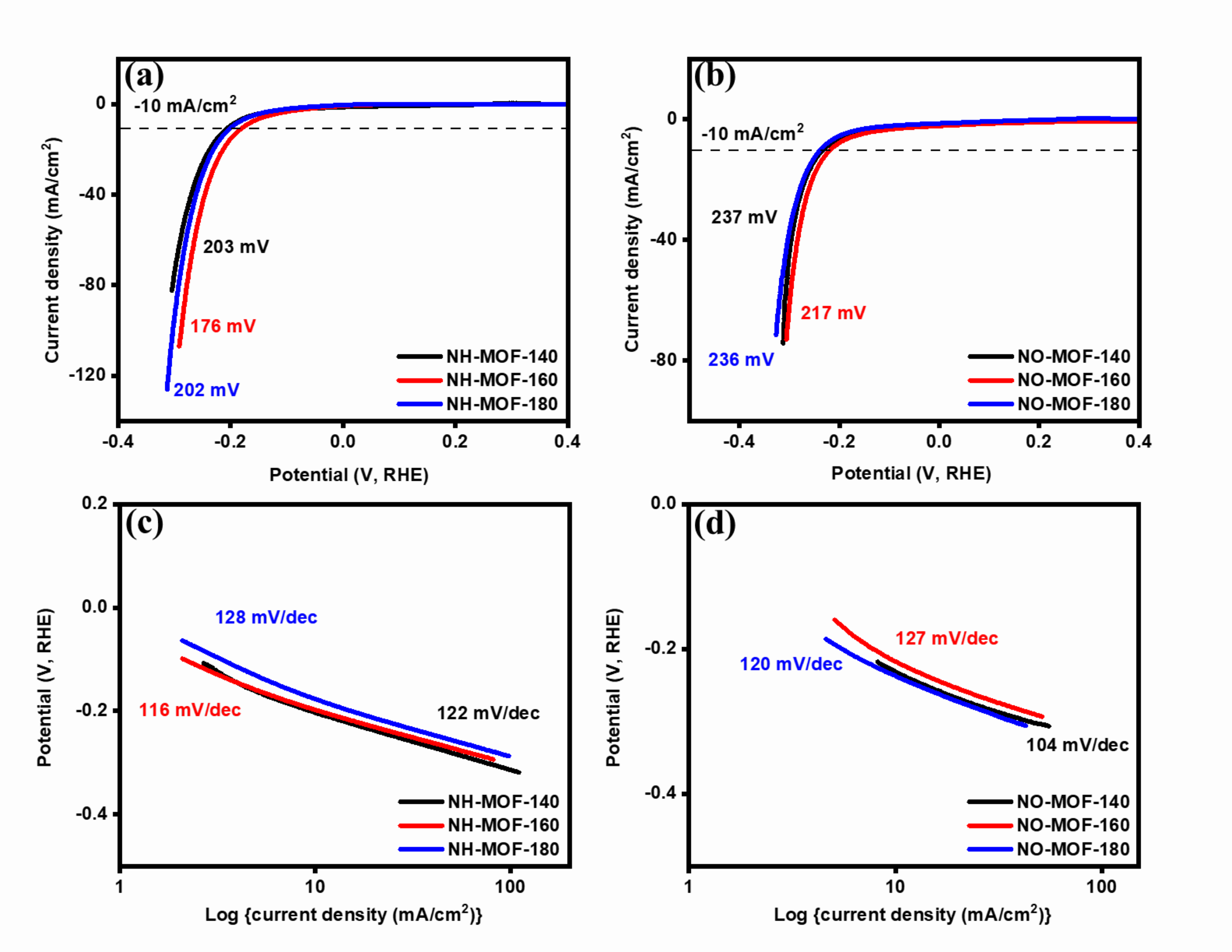

Figure 23: (a-b) HER polarization curves; (c-d) Tafel slope of NH-MOF; and NO-MOF based samples.

In addition, the electrocatalytic behavior of the as-prepared MOFs was analyzed using Turnover frequency (TOF), which explains how rapidly a catalyst can turn reactants into products per unit of time at a specific overpotential (rate of reaction). Equation 19 was used to calculate the value of TOFs.

$$TOF = \frac{jN_a}{nF\tau} \qquad \text{eq. 19}$$

where N_a is Avogadro's number, n is the number of electrons transferred to molecule of the product (for HER n=2), and τ is the number of atoms of catalyst material that take part in the chemical reaction (the surface concentration of active sites), F is Faraday's constant, and j is the current density. The TOF for all the NH-MOFs and NO-MOFs are shown in **Figure 24(a-b)**; the NH-MOF-160 showed 52 sec^{-1} and NO-MOF-160 exhibited 180 sec^{-1} [79]. The above polarization, Tafel, and TOF results are supported through EIS, where Nyquist plots determine the ESR (R_s) on real axis intercept. The best NH-MOF-160 and NO-MOF-160 show 1.76 and 2.18 Ω of R_s, as shown in **Figure 24(c-d)**.

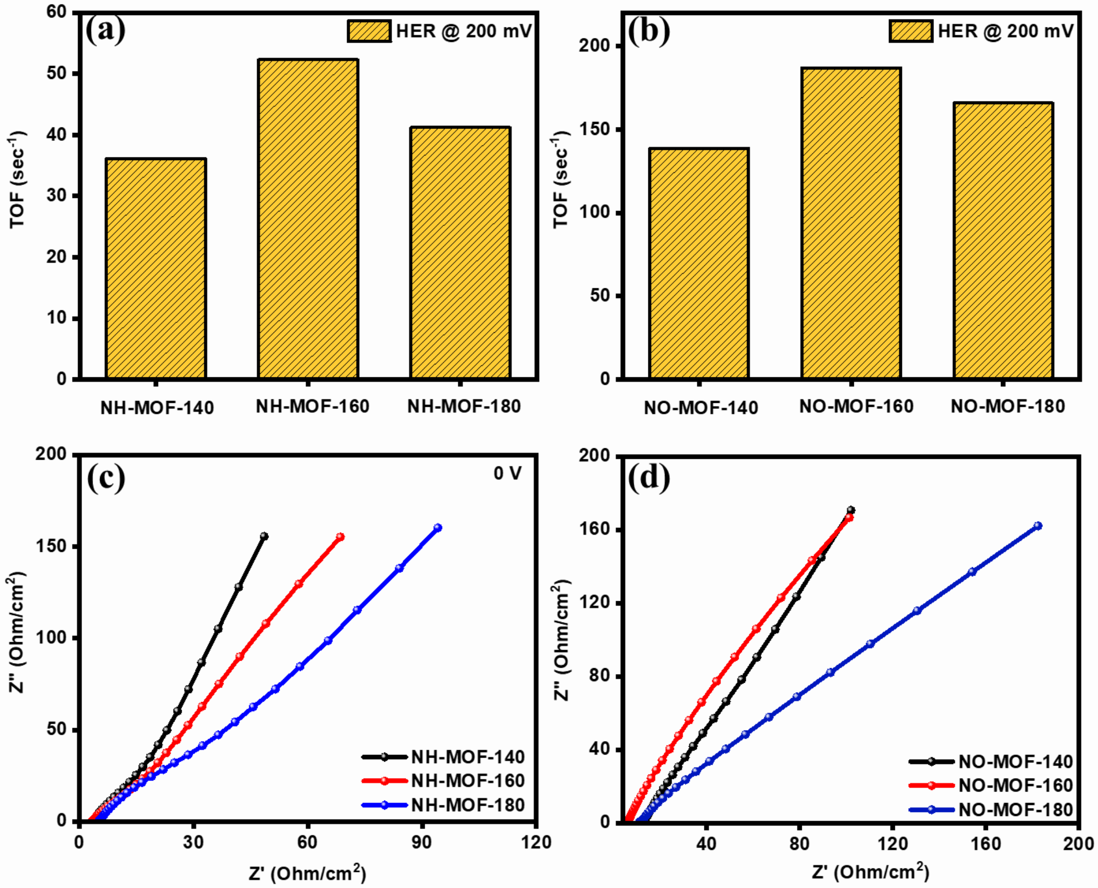

Figure 24: (a-b) TOF of NH-MOF; and NO-MOF based samples; (c-d) Nyquist plot of NH-MOF; and NO-MOF based samples at 0 V versus Ag/AgCl.

The HER stability of an electrocatalyst is vital. LSV CV- cycle 1 and 1k of all the as-prepared MOFs overlap, proving their stability for the long run. The NH-MOF-160 and NO-MOF-160 exhibit the highest current density of 126 and 93 mA/cm^2, as shown in **Figure 25**.

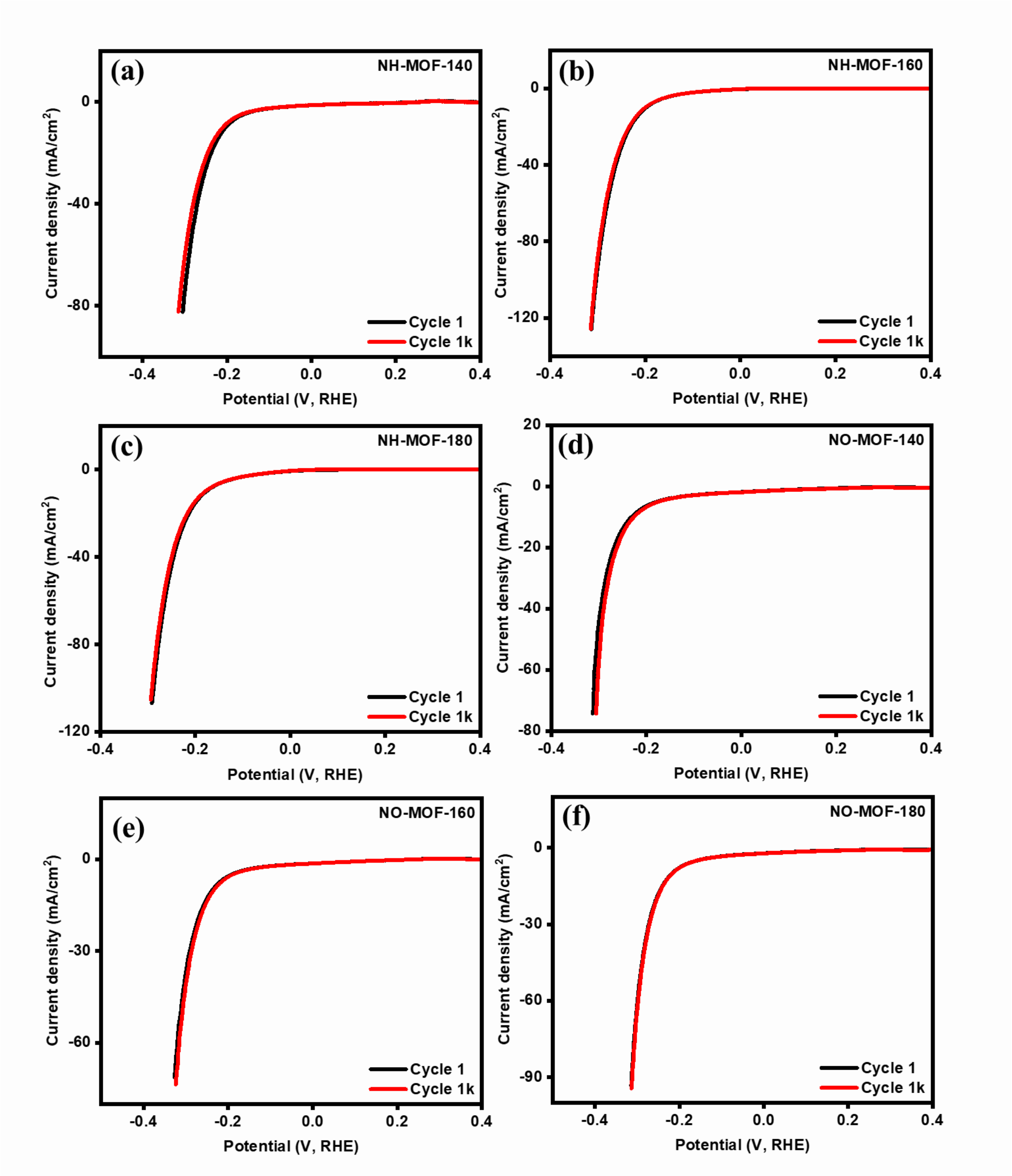

Figure 25: LSV CV curves of cycle 1 and 1k of NH-MOF; and NO-MOF based samples.

Polarization curves were used for all as-prepared MOFs to understand the OER activity (**Figure 27(a-b)**). The OER occurs at the surface of active metal sites and is shown by equation 9(a-e). To reach a current density of 10 mA/cm^2, NH-MOF-160 required an overpotential of 268 mV, while NO-MOF-160 required an overpotential of 332 mV. The reaction kinetics of as-prepared MOFs were calculated using a Tafel plot, as shown in **Figure 26(c-d)**. The NH-MOF-160 and NO-MOF-160 exhibited the lowest Tafel slope of 86 and 93 mV/dec, indicating faster reaction kinetics for NH-MOF-160 [80].

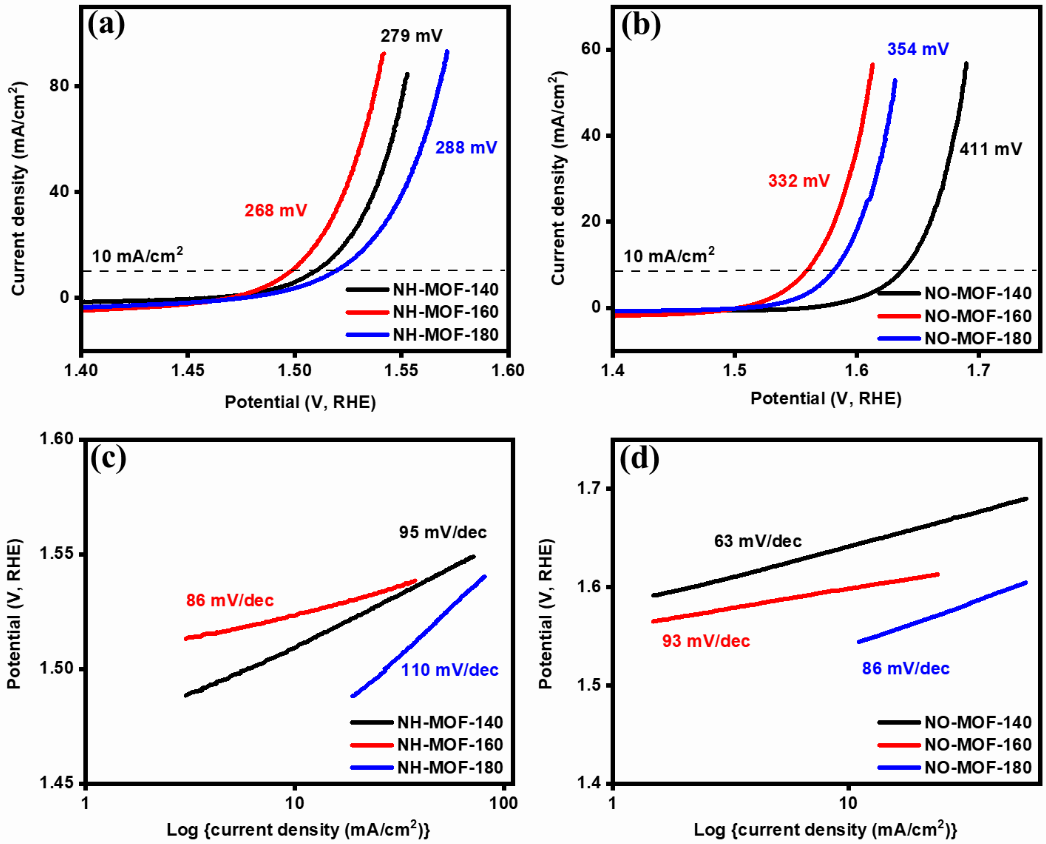

Figure 26: (a-b) OER polarization curves of NH-MOF; and NO-MOF based samples; (c-d) Tafel slope of NH-MOF; and NO-MOF based samples.

To confirm the above results, TOF graphs were plotted (**Figure 27**). NH-MOF-160 and NO-MOF-160 exhibit the highest TOF of 92 and 78 sec^{-1} at an overpotential of 300 mV.

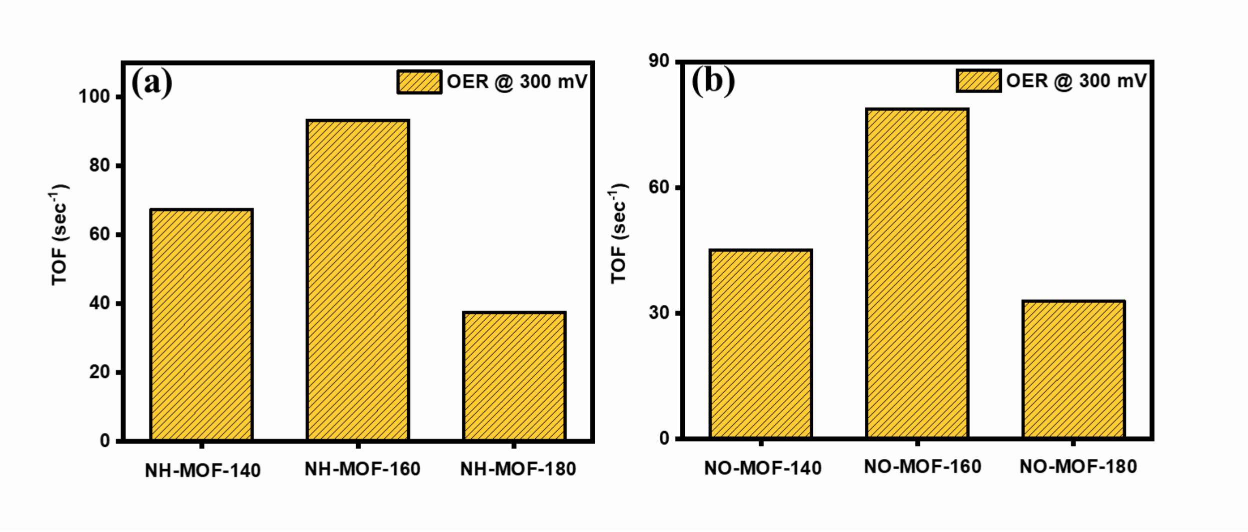

Figure 27: TOF of (a) NH-MOF; and (b) NO-MOF based samples at 300 mV overpotentials.

Nyquist plots can be used to study the ionic movement. The charge transfer resistance (R_{ct}) of as-prepared MOFs was calculated through the semicircular region in a high-frequency range, and ESR was depicted on the intercept at the real axis. NH-MOF-160 showed the lowest R_s of 1.73 Ω, and NO-MOF-160 showed R_s of 2.06 Ω which is directly corelated to their ionic movement as shown in **Figure 28**.

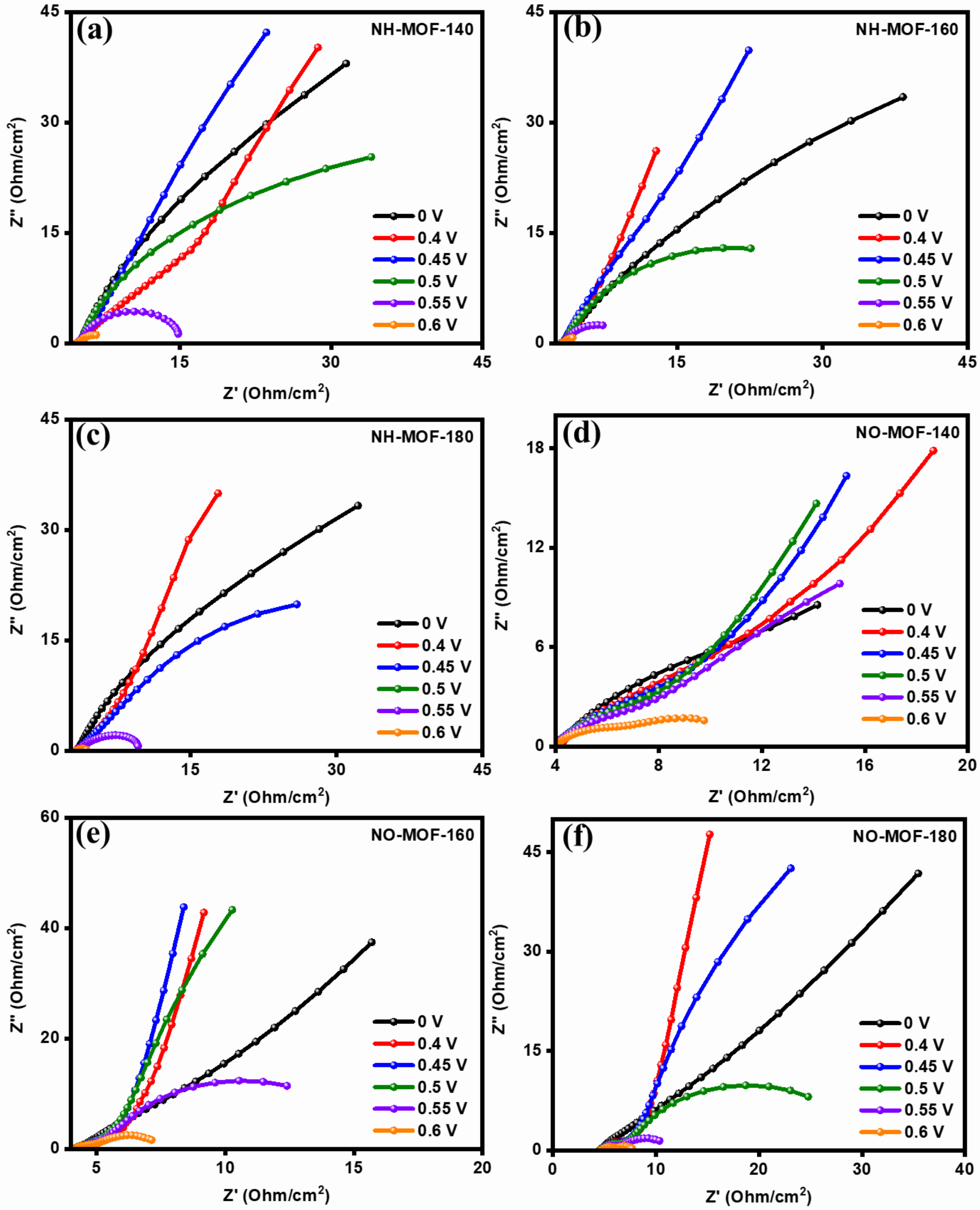

Figure 28: Nyquist plots of NH-MOF; and NO-MOF based samples at various potentials.

The kinetic mechanism was explored after recording CV curves at various scan rates. These CV curves were used to calculate the double capacitance (C_{dl}) of the non-faradaic region and directly correlate with the electrochemical active surface area (ECSA). Also, the slope of the scan rate (mV/sec) versus current (mA) graph results in C_{dl} and is shown by equation 20(a).

$$I_c = vC_{dl} \qquad \text{eq. 20(a)}$$

where v is the scan rate I_c is the peak current, and C_{dl} is the double layer capacitance [81]. The NH-MOF-160 and NO-MOF-160 exhibit the 6.3 and 9.5 mF of C_{dl} (as shown in **Figure 29(a-b)**). ECSA was calculated using equation 20(b), in which the C_s remains fixed with 0.04 mF.

$$\text{ECSA} = C_{dl}/C_s \qquad \text{eq. 20(b)}$$

The ECSA curve for both MOFs is shown in **Figure 29(c-d)**. Moreover, the higher value of ECSA corresponds to the roughness factor (RF), calculated using above equation 20(c),

$$\text{RF} = \text{ECSA}/\text{GSA} \qquad \text{eq. 20(c)}$$

in which GSA referred geometrically activated surface area [82]. The NH-MOF-160 and NO-MOF-160 exhibited the RF of 300 and 650 as shown in **Figure 29(e-f)**.

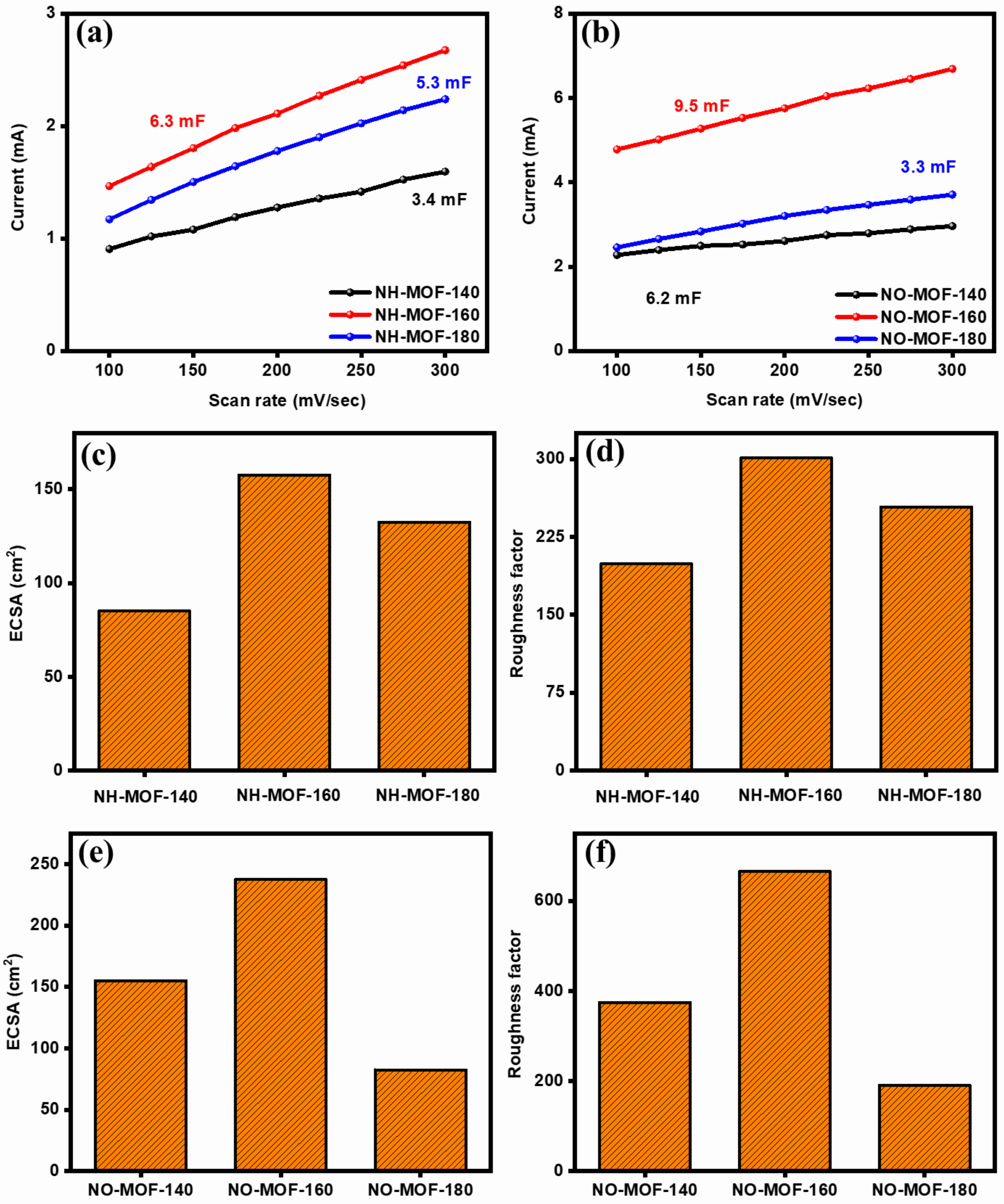

Figure 29: (a-b) Scan rate v/s current curve of NH-MOF; and NO-MOF based samples; (c-f) ECSA and RF of NH-MOF; and NO-MOF based samples.

The performance of these MOFs could be attributed to their morphology. NH-MOF-140 exhibited the agglomerated particles attached to a thick sheet, providing a low surface area for ions to perform redox reactions. Although agglomeration happened in the NH-MOF-160, its flat surface provided more active sites, allowing more surface reactions and explaining its better performance compared to other as-prepared MOFs [83]. As the temperature of preparation increased, irregularly distorted particles were formed, preventing ions from attacking the surface of the electrode and reducing its performance. Moreover, the calcined NH-MOFs turned into NO-MOFs where the particles seem to be highly agglomerated, providing instability which in turn reduces the results of the NO-MOFs.

All the as-prepared MOFs exhibited the polarization curve for stability through cycle 1 and cycle 1k as shown in **Figure 30**. In addition, to analyze the stability of MOFs, *i-t* curves were observed through a chronoamperometry (CA) experiment for 24 h. CA showed a minimal loss in current density over the continuous period, as shown in **Figure 31**.

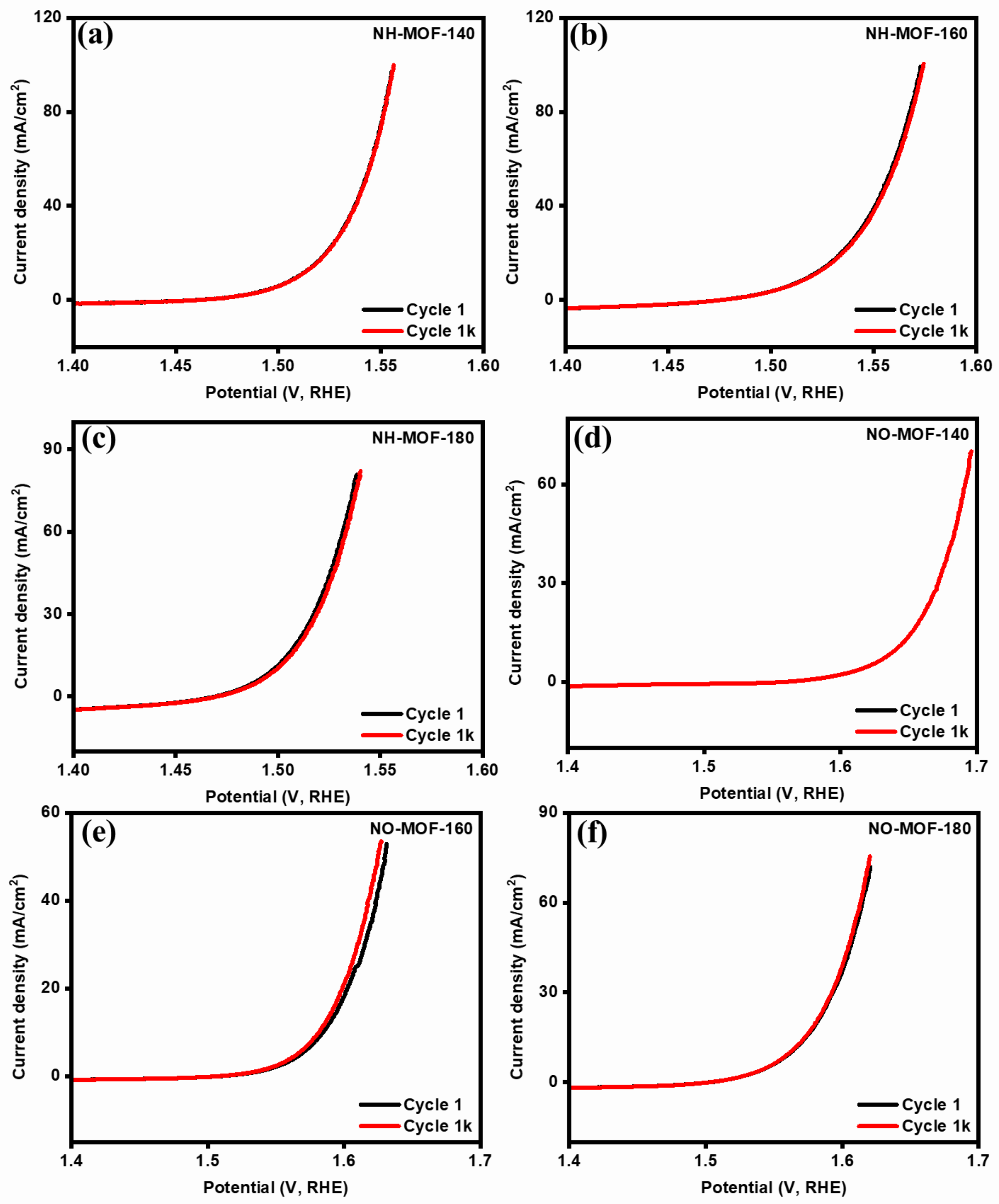

Figure 30: LSV CV curves for cycle 1 and 1k of NH-MOF; and NO-MOF based samples.

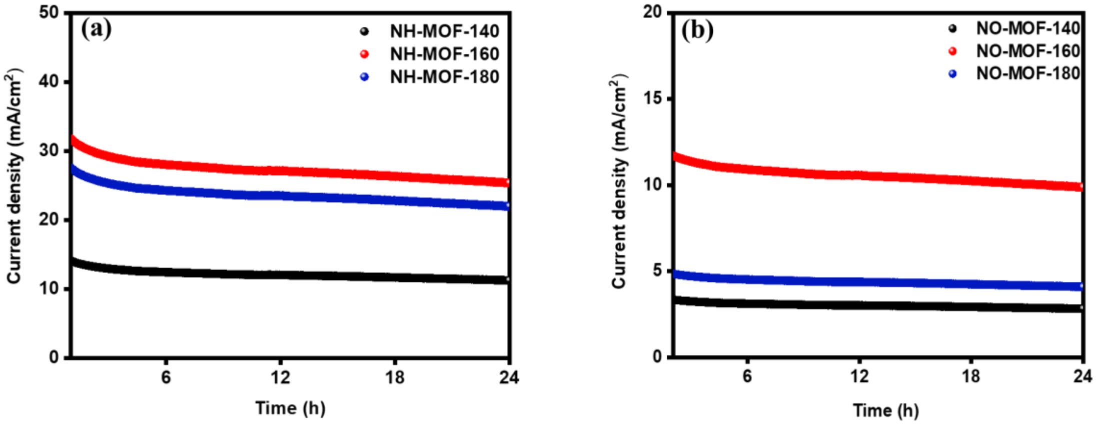

Figure 31: Chronoamperometry plot of (a) NH-MOF; and (b) NO-MOF based samples.

Table 2. Comparison between various data of water splitting.

Sample name	**OER** **Overpotential@10 mA/cm^2**	**HER** **Overpotential@10 mA/cm^2**	**Reference**
NFF	452	-	[84]
NCN@ZIF	402	-	[84]
NCO@C	342	156	[84]
Ni/Co-DH	273	187	[85]
CF-CFO/NC	243	-	[86]
NiCo-UMOFNs	280	182	[87]
NH-MOF-160	**268**	**176**	**This work**
NH-MOF-180	**279**	**202**	**This work**

3.2.3 Electrolyzer testing

The excellent electrocatalytic properties of NH-MOF-160 among all as-prepared MOFs allowed us to investigate its real-life application through electrolyzer testing. The electrolyzer consists of two same electrodes (NH-MOF-160||NH-MOF-160) of an electrocatalyst, where one acts as the cathode and the other as an anode, assembled in 1M KOH [88]. The activity of the electrolyzer is represented through polarization curve where NH-MOF-160 required 575 mV to reach a current density of 10 mA/cm^2 as shown in **Figure 32(a)**. Moreover, the stability of the device was demonstrated through the LSV CV curves between cycle 1 and cycle 1k with almost no deviation, as shown in **Figure 32(b)**. Also, the Nyquist plot in **Figure 32(c)**, where its R_s is 3.2 Ω, shows excellent electrocatalytic properties. The long-term stability of the electrolyzer was observed through CA testing for 24 h as shown in **Figure 32(d)**.

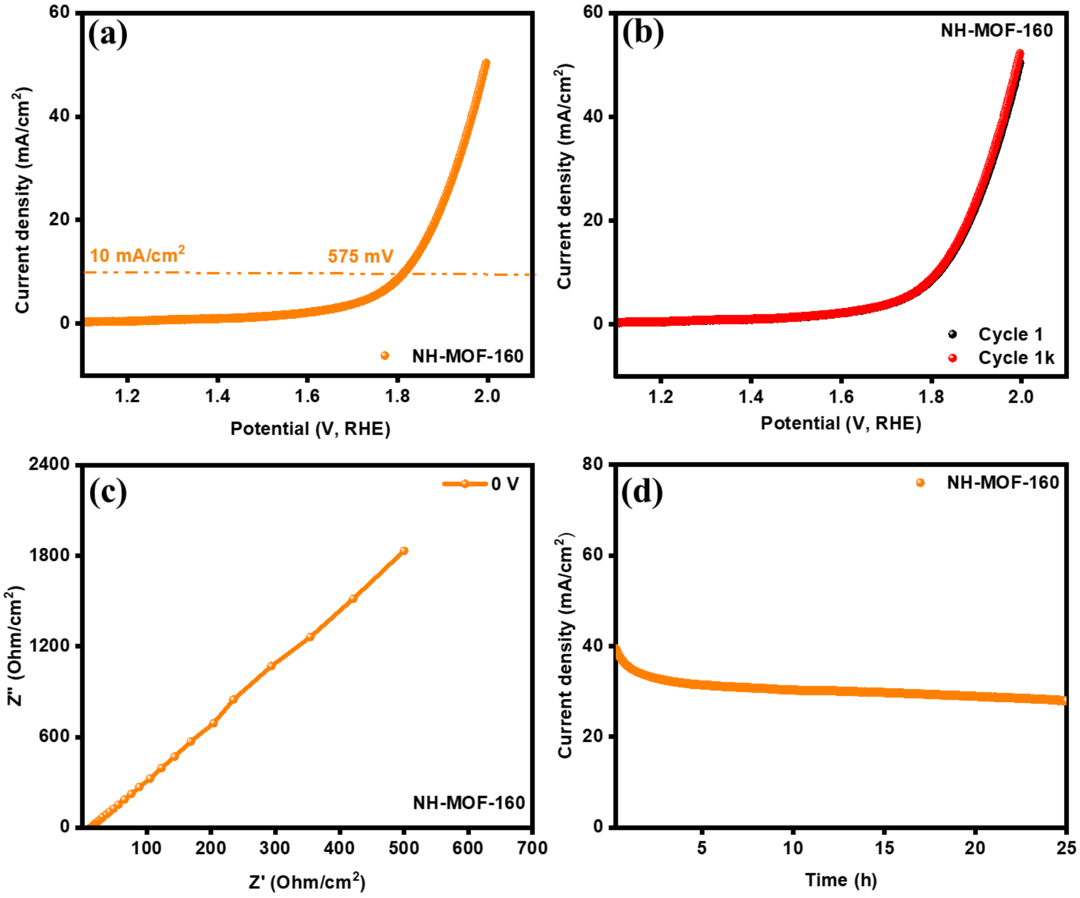

Figure 32: (a) OER polarization curve for NH-MOF-160; (b) LSV CV for cycle 1 and 1k of NH-MOF-160; (c) Nyquist plot for electrolyzer device; (d) current density v/s time curve over 24 h for NH-MOF-160.

CHAPTER IV

CONCLUSION

NH-MOFs and NO-MOFs were prepared successfully using hydrothermal synthesis route at various temperatures. All the as-prepared MOFs exhibited a highly crystalline nature. The effect of temperature was observed on the morphology of MOFs, which can be seen in SEM images at different magnification levels. Moreover, FT-IR confirms the OH^- stretching bond of hydroxide-based MOFs. Elemental mapping confirmed the uniform distribution of elements in as-prepared MOFs. NH-MOFs exhibited superior SC properties with highest C_{sp} of 608 F/g at 1 A/g corresponding to 1482 F/g at 2 mV/sec of scan rate. However, NH-MOF-160 possessed the lowest possible R_s of 0.96 Ω, allowing more conduction of ions. Also, NH-MOF-160 exhibited the highest retention in capacitance (more than 97% at current density of 10 A/g). All the as-prepared MOFs exhibited advanced electrocatalytic properties, among which NH-MOF-160 showed the best performance due to its flat rock morphology, which in turn allows more charges to accumulate on the surface of its electrode. NH-MOF-160 required an OER overpotential of 268 mV to reach a current density of 10 mA/cm^2 with fastest kinetics calculated through Tafel slope of 86 mV/dec. For HER NH-MOF-160 required only 176 mV to attain a current density of 10 mA/cm^2 with Tafel slope of 116 mV/dec. The excellent performance of NH-MOF-160 encouraged checking real-life application through an electrolyzer device. The device required 0.575 V of overpotential to reach a current density of 10 mA/cm^2. NH-MOF-160 also showed high stability, through LSV CV curves overlapping, and exhibited highly stable current density of 36 mA/cm^2 for 24 h.

REFERENCES

[1] S. Koohi-Fayegh, M.A. Rosen, A review of energy storage types, applications and recent developments, J. Energy Storage. 27 (2020) 101047.

[2] X. Luo, J. Wang, M. Dooner, J. Clarke, Overview of current development in electrical energy storage technologies and the application potential in power system operation, Appl. Energy. 137 (2015) 511–536.

[3] M.M. Rahman, A.O. Oni, E. Gemechu, A. Kumar, Assessment of energy storage technologies: A review, Energy Convers. Manag. 223 (2020) 113295.

[4] D. Kasprzak, C.C. Mayorga-Martinez, M. Pumera, Sustainable and Flexible Energy Storage Devices: A Review, Energy and Fuels. 37 (2023) 74–97.

[5] Z. Zhu, T. Jiang, M. Ali, Y. Meng, Y. Jin, Y. Cui, W. Chen, Rechargeable Batteries for Grid Scale Energy Storage, Chem. Rev. 122 (2022) 16610–16751.

[6] V. Kale, M. Secanell, A comparative study between optimal metal and composite rotors for flywheel energy storage systems, Energy Reports. 4 (2018) 576–585.

[7] J. Wang, K. Lu, L. Ma, J. Wang, M. Dooner, S. Miao, J. Li, D. Wang, Overview of compressed air energy storage and technology development, Energies. 10 (2017) 991.

[8] H.L. Ferreira, R. Garde, G. Fulli, W. Kling, J.P. Lopes, Characterisation of electrical energy storage technologies, Energy. 53 (2013) 288–298.

[9] M. Kintner-Meyer, C. Jin, P. Balducci, M. Elizondo, X. Guo, T. Nguyen, F. Tuffner, V. Viswanathan, Energy storage for variable renewable energy resource integration

— A regional assessment for the Northwest Power Pool (NWPP), in: 2011 IEEE/PES Power Syst. Conf. Expo., 2011: pp. 1–7.

[10] J. Wang, Z. Yang, S. Liu, Q. Zhang, Y. Han, A comprehensive overview of hybrid construction machinery, Adv. Mech. Eng. 8 (2016) 1687–1709.

[11] M. Tomy, A. Ambika Rajappan, V. VM, X. Thankappan Suryabai, Emergence of Novel 2D Materials for High-Performance Supercapacitor Electrode Applications: A Brief Review, Energy and Fuels. 35 (2021) 19881–19900.

[12] N. Du, C. Roy, R. Peach, M. Turnbull, S. Thiele, C. Bock, Anion-Exchange Membrane Water Electrolyzers, Chem. Rev. 122 (2022) 11830–11895.

[13] P.J. Hall, E.J. Bain, Energy-storage technologies and electricity generation, Energy Policy. 36 (2008) 4352–4355.

[14] G. Wang, Z. Lu, Y. Li, L. Li, H. Ji, A. Feteira, D. Zhou, D. Wang, S. Zhang, I.M. Reaney, Electroceramics for High-Energy Density Capacitors: Current Status and Future Perspectives, Chem. Rev. 121 (2021) 6124–6172.

[15] Y. Shao, M.F. El-Kady, J. Sun, Y. Li, Q. Zhang, M. Zhu, H. Wang, B. Dunn, R.B. Kaner, Design and Mechanisms of Asymmetric Supercapacitors, Chem. Rev. 118 (2018) 9233–9280.

[16] D.C. Grahame, The thermodynamic theory of electrocapillarity The kinetic theory of the diffuse double layer The theory of the compact double layer Potential differenc, Philos. Mag. Ser. 6. (1947) 441–501.

[17] B.E. Conway, Transition from “supercapacitor” to “battery” behavior in

electrochemical energy storage, Proc. Int. Power Sources Symp. (1991) 319–327.

[18] M. Winter, R.J. Brodd, What are batteries, fuel cells, and supercapacitors?, Chem. Rev. 104 (2004) 4245–4269.

[19] J.R. Miller, P. Simon, Electrochemical Capacitors for Energy Management, Science (80-.). 321 (2008) 651–652.

[20] D.R. Rolison, J.W. Long, J.C. Lytle, A.E. Fischer, C.P. Rhodes, T.M. McEvoy, M.E. Bourg, A.M. Lubers, Multifunctional 3D nanoarchitectures for energy storage and conversion, Chem. Soc. Rev. 38 (2009) 226–252.

[21] L. Guo, J. Tan, W. Li, G. Hu, S. Zhang, Underpotential deposition, Prog. Chem. 25 (2013) 1842–1857.

[22] L. Zhang, X.S. Zhao, Carbon-based materials as supercapacitor electrodes, Chem. Soc. Rev. 38 (2009) 2520–2531.

[23] V. Augustyn, P. Simon, B. Dunn, Pseudocapacitive oxide materials for high-rate electrochemical energy storage, Energy Environ. Sci. 7 (2014) 1597–1614.

[24] P. Simon, Y. Gogotsi, Materials for electrochemical capacitors, Nat. Mater. 7 (2008) 845–854.

[25] V. Augustyn, J. Come, M.A. Lowe, J.W. Kim, P.L. Taberna, S.H. Tolbert, H.D. Abruña, P. Simon, B. Dunn, High-rate electrochemical energy storage through Li + intercalation pseudocapacitance, Nat. Mater. 12 (2013) 518–522.

[26] W. Zhang, M. Liu, X. Gu, Y. Shi, Z. Deng, N. Cai, Water Electrolysis toward Elevated Temperature: Advances, Challenges and Frontiers, Chem. Rev. 2 (2022)

9–127.

[27] B. Pivovar, Catalysts for fuel cell transportation and hydrogen related uses, Nat. Catal. 2 (2019) 562–565.

[28] A. Basile, S. Liguori, A. Iulianelli, 2 - Membrane reactors for methane steam reforming (MSR), in: A. Basile, L. Di Paola, F. l. Hai, V.B.T.-M.R. for E.A. and B.C.P. Piemonte (Eds.), Woodhead Publ. Ser. Energy, Woodhead Publishing, 2015: pp. 31–59.

[29] D.P. Harrison, Sorption-enhanced hydrogen production: A review, Ind. Eng. Chem. Res. 47 (2008) 6486–6501.

[30] C. Higman, S. Tam, Advances in coal gasification, hydrogenation, and gas treating for the production of chemicals and fuels, Chem. Rev. 114 (2014) 1673–1708.

[31] P. Mondal, G.S. Dang, M.O. Garg, Syngas production through gasification and cleanup for downstream applications - Recent developments, Fuel Process. Technol. 92 (2011) 1395–1410.

[32] Z. Li, P. Wei, G. Wang, Recent Advances on Perovskite Electrocatalysts for Water Oxidation in Alkaline Medium, Energy and Fuels. 36 (2022) 11724–11744.

[33] M.A. Khan, H. Zhao, W. Zou, Z. Chen, W. Cao, J. Fang, J. Xu, L. Zhang, J. Zhang, Recent Progresses in Electrocatalysts for Water Electrolysis, Electrochem. Energy Rev. 1 (2018) 483–530.

[34] D. Yao, L. Gu, B. Zuo, S. Weng, S. Deng, W. Hao, A strategy for preparing high-efficiency and economical catalytic electrodes toward overall water splitting,

Nanoscale. 13 (2021) 10624–10648.

[35] N. Du, C. Roy, R. Peach, M. Turnbull, S. Thiele, C. Bock, Anion-Exchange Membrane Water Electrolyzers, Chem. Rev. 122 (2022) 11830–11895.

[36] S. Lokesh, R. Srivastava, Advanced Two-Dimensional Materials for Green Hydrogen Generation: Strategies toward Corrosion Resistance Seawater Electrolysis─Review and Future Perspectives, Energy and Fuels. 36 (2022) 13417–13450.

[37] A.M.R. Ramírez, S. Heidari, A. Vergara, M.V. Aguilera, P. Preuss, M.B. Camarada, A. Fischer, Rhenium-Based Electrocatalysts for Water Splitting, ACS Mater. Au. 28 (2023) 3221–3236.

[38] Z. Shi, X. Wang, J. Ge, C. Liu, W. Xing, Fundamental understanding of the acidic oxygen evolution reaction: Mechanism study and state-of-the-art catalysts, Nanoscale. 12 (2020) 13249–13275.

[39] C. Hu, L. Zhang, J. Gong, Recent progress made in the mechanism comprehension and design of electrocatalysts for alkaline water splitting, Energy Environ. Sci. 12 (2019) 2620–2645.

[40] X. Zou, Y. Zhang, Noble metal-free hydrogen evolution catalysts for water splitting, Chem. Soc. Rev. 44 (2015) 5148–5180.

[41] J. Rossmeisl, Z.-W. Qu, H. Zhu, G.-J. Kroes, J.K. Nørskov, Electrolysis of water on oxide surfaces, J. Electroanal. Chem. 607 (2007) 83–89.

[42] J. Liu, J. Wang, C. Xu, H. Jiang, C. Li, L. Zhang, J. Lin, Z.X. Shen, Advanced

Energy Storage Devices: Basic Principles, Analytical Methods, and Rational Materials Design, Adv. Sci. 5 (2018) 17003–17022.

[43] X. Zhou, Y. Qin, X. He, Q. Li, J. Sun, Z. Lei, Z.-H. Liu, Ti3C2Tx Nanosheets/Ti3C2Tx Quantum Dots/RGO (Reduced Graphene Oxide) Fibers for an All-Solid-State Asymmetric Supercapacitor with High Volume Energy Density and Good Flexibility, ACS Appl. Mater. Interfaces. 12 (2020) 11833–11842.

[44] M. Guan, Q. Wang, X. Zhang, J. Bao, X. Gong, Y. Liu, Two-Dimensional Transition Metal Oxide and Hydroxide-Based Hierarchical Architectures for Advanced Supercapacitor Materials, Front. Chem. 8 (2020) 1–14.

[45] J. Zhang, L.-B. Kong, J.-J. Cai, H. Li, Y.-C. Luo, L. Kang, Hierarchically porous nickel hydroxide/mesoporous carbon composite materials for electrochemical capacitors, Microporous Mesoporous Mater. 132 (2010) 154–162.

[46] T.-F. Yi, J. Mei, B. Guan, P. Cui, S. Luo, Y. Xie, Y. Liu, Construction of spherical NiO@MnO2 with core-shell structure obtained by depositing MnO2 nanoparticles on NiO nanosheets for high-performance supercapacitor, Ceram. Int. 46 (2020) 421–429.

[47] O.M. Yaghi, H. Li, Hydrothermal Synthesis of a Metal-Organic Framework Containing Large Rectangular Channels, J. Am. Chem. Soc. 117 (1995) 10401–10402.

[48] M. Kondo, T. Yoshitomi, H. Matsuzaka, S. Kitagawa, K. Seki, Three-Dimensional Framework with Channeling Cavities for Small Molecules: {[M2(4, 4′-bpy)3(NO3)4]·xH2O}n (M-Co, Ni, Zn), Angew. Chemie Int. Ed. English. 36 (1997)

1725–1727.

[49] M.S. Khan, M. Shahid, Synthesis of metal-organic frameworks (MOFs): Routes to various MOF topologies, morphologies, and composites, Electrochem. Appl. Met. Fram. Adv. Futur. Potential. 7 (2022) 17–35.

[50] J. Xu, S. Liu, Y. Liu, Co3O4/ZnO nanoheterostructure derived from core–shell ZIF-8@ZIF-67 for supercapacitors, RSC Adv. 6 (2016) 52137–52142.

[51] F.-L. Li, Q. Shao, X. Huang, J.-P. Lang, Nanoscale Trimetallic Metal–Organic Frameworks Enable Efficient Oxygen Evolution Electrocatalysis, Angew. Chemie Int. Ed. 57 (2018) 1888–1892.

[52] T. Qiu, Z. Liang, W. Guo, H. Tabassum, S. Gao, R. Zou, Metal–Organic Framework-Based Materials for Energy Conversion and Storage, ACS Energy Lett. 5 (2020) 520–532.

[53] A.A. Bunaciu, E. gabriela Udriştioiu, H.Y. Aboul-Enein, X-Ray Diffraction: Instrumentation and Applications, Crit. Rev. Anal. Chem. 45 (2015) 289–299.

[54] C.W. Oatley, The early history of the scanning electron microscope, J. Appl. Phys. 53 (1982) R1–R13.

[55] V.-D. Hodoroaba, Chapter 4.4 - Energy-dispersive X-ray spectroscopy (EDS), in: V.-D. Hodoroaba, W.E.S. Unger, A.G.B.T.-C. of N. Shard (Eds.), Micro Nano Technol., Elsevier, 2020: pp. 397–417.

[56] M.K. Singh, A. Singh, Chapter 13 - Fourier transform infrared (FTIR) analysis, in: M.K. Singh, A.B.T.-C. of P. and F. Singh (Eds.), Text. Inst. B. Ser., Woodhead

Publishing, 2022: pp. 295–320.

[57] Y. Liu, G. Mou, Y. Wang, F. He, N. Dong, Y. Lin, M. Zhong, B. Su, Nickel/Nickel Oxide-Nitrogen Self-Doped Carbon Nanosheets for Electrocatalytic Oxygen and Hydrogen Evolution Reactions, ACS Appl. Nano Mater. 5 (2022) 2953–2961.

[58] C. Mukarakate, A. Mittal, P.N. Ciesielski, S. Budhi, L. Thompson, K. Iisa, M.R. Nimlos, B.S. Donohoe, Influence of crystal allomorph and crystallinity on the products and behavior of cellulose during fast pyrolysis, ACS Sustain. Chem. Eng. 4 (2016) 4662–4674.

[59] L.M. Cao, Q.C. Cao, J. Zhang, X.Y. Zhu, R.Z. Sun, Z.Y. Du, C.T. He, Electrochemically Controlled Synthesis of Ultrathin Nickel Hydroxide Nanosheets for Electrocatalytic Oxygen Evolution, Inorg. Chem. 60 (2021) 3365–3374.

[60] P.E. Lokhande, K. Pawar, U.S. Chavan, Chemically deposited ultrathin α-Ni(OH)2 nanosheet using surfactant on Ni foam for high performance supercapacitor application, Mater. Sci. Energy Technol. 1 (2018) 166–170.

[61] M. El-Kemary, N. Nagy, I. El-Mehasseb, Nickel oxide nanoparticles: Synthesis and spectral studies of interactions with glucose, Mater. Sci. Semicond. Process. 16 (2013) 1747–1752.

[62] R. Liang, Y. Du, J. Lin, J. Chen, P. Xiao, Facile-Synthesized Ni-Metal-Organic Framework/Nano Carbon Electrode Material for High-Performance Supercapacitors, Energy and Fuels. 36 (2022) 7115–7120.

[63] S. Liu, Y.Y. Sun, Y.P. Wu, Y.J. Wang, Q. Pi, S. Li, Y.S. Li, D.S. Li, Common

Strategy: Mounting the Rod-like Ni-Based MOF on Hydrangea-Shaped Nickel Hydroxide for Superior Electrocatalytic Methanol Oxidation Reaction, ACS Appl. Mater. Interfaces. 13 (2021) 26472–26481.

[64] Z. Li, Q. Ma, H. Zhang, Q. Zhang, K. Zhang, H. Mei, B. Xu, D. Sun, Self-Assembly of Metal-Organic Frameworks on Graphene Oxide Nanosheets and In Situ Conversion into a Nickel Hydroxide/Graphene Oxide Battery-Type Electrode, Inorg. Chem. 61 (2022) 12129–12137.

[65] Y. Budipramana, Suprapto, T. Ersam, F. Kurniawan, Synthesis nickel hidroxide by electrolysis at high voltage, ARPN J. Eng. Appl. Sci. 9 (2014) 2074–2077.

[66] C. Xu, W. Yang, J. Zhao, J. Ma, M. Wu, Designing Multifunctional Co and Fe Co-Doped MoS2Nanocube Electrodes for Dye-Sensitized Solar Cells, Perovskite Solar Cells, and a Supercapacitor, ACS Omega. 6 (2021) 24931–24939.

[67] J. Choi, T. Ingsel, D. Neupane, S.R. Mishra, A. Kumar, R.K. Gupta, Metal-organic framework-derived cobalt oxide and sulfide having nanoflowers architecture for efficient energy conversion and storage, J. Energy Storage. 50 (2022) 104145.

[68] D. Guragain, C. Zequine, R. Bhattarai, J. Choi, R.K. Gupta, X. Shen, S.R. Mishra, Effect of dopant on the morphology and electrochemical performance of Ni1-xCaxCo2O4 (0 = x = 0.8) oxide hierarchical structures, MRS Adv. 5 (2020) 2487–2494.

[69] R. Srivastava, S. Bhardwaj, A. Kumar, R. Singhal, J. Scanley, C.C. Broadbridge, R.K. Gupta, Waste Citrus reticulata Assisted Preparation of Cobalt Oxide Nanoparticles for Supercapacitors, Nanomaterials. 12 (2022) 4119–4132.

[70] Y. Liu, X. Li, M. Gao, X. Hao, J. Li, Y. Liu, Y. Li, K. Cai, High-Energy-Density Asymmetric Supercapacitor Based on a Nickel Cobalt Double Hydroxide/Reduced-Graphene-Oxide Fiber Electrode, ACS Appl. Energy Mater. 5 (2022) 9605–9615.

[71] H. Chen, S. Zhou, L. Wu, Porous nickel hydroxide-manganese dioxide-reduced graphene oxide ternary hybrid spheres as excellent supercapacitor electrode materials, ACS Appl. Mater. Interfaces. 6 (2014) 8621–8630.

[72] S. Gao, Y. Sui, F. Wei, J. Qi, Q. Meng, Y. Ren, Y. He, Dandelion-like nickel/cobalt metal-organic framework based electrode materials for high performance supercapacitors, J. Colloid Interface Sci. 531 (2018) 83–90.

[73] X. Zhang, J. Wang, X. Ji, Y. Sui, F. Wei, J. Qi, Q. Meng, Y. Ren, Y. He, D. Zhuang, Flake-like nickel/cobalt metal-organic framework as high-performance electrodes for supercapacitors, J. Mater. Sci. Mater. Electron. 31 (2020) 16260–16268.

[74] F. Ren, Y. Ji, F. Chen, Y. Qian, J. Tian, J. Wang, Flower-like bimetal Ni/Co-based metal–organic-framework materials with adjustable components toward high performance solid-state supercapacitors, Mater. Chem. Front. 5 (2021) 7333–7342.

[75] S. Zhao, L. Zeng, G. Cheng, L. Yu, H. Zeng, Ni/Co-based metal-organic frameworks as electrode material for high performance supercapacitors, Chinese Chem. Lett. 30 (2019) 605–609.

[76] K.M. Choi, H.M. Jeong, J.H. Park, Y.-B. Zhang, J.K. Kang, O.M. Yaghi, Supercapacitors of Nanocrystalline Metal–Organic Frameworks, ACS Nano. 8 (2014) 7451–7457.

[77] A.L. Pauls, M.T.Y. Paul, R.F. Ali, B.D. Gates, Gel-like State of Nickel Hydroxide Created by Electrochemical Aging under Alkaline Conditions, ACS Appl. Energy Mater. 4 (2021) 10668–10681.

[78] D. Wei, L. Chen, L. Tian, S. Ramakrishna, D. Ji, Hierarchically Structured CoNiP/CoNi Nanoparticle/Graphene/Carbon Foams as Effective Bifunctional Electrocatalysts for HER and OER, Ind. Eng. Chem. Res. 62 (2023) 4987–4994.

[79] D. Rathore, S. Ghosh, J. Chowdhury, S. Pande, Co-Doped Ni9S8 Nanostructures for Electrocatalytic Water Splitting over a Wide pH Range, ACS Appl. Nano Mater. 5 (2022) 11823–11838.

[80] T. Priamushko, P. Guggenberger, A. Mautner, J. Lee, R. Ryoo, F. Kleitz, Enhancing OER Activity of Ni/Co Oxides via Fe/Mn Substitution within Tailored Mesoporous Frameworks, 5 (2022) 13385–13397.

[81] W. Zhou, D.-D. Huang, Y.-P. Wu, J. Zhao, T. Wu, J. Zhang, D.-S. Li, C. Sun, P. Feng, X. Bu, Stable Hierarchical Bimetal–Organic Nanostructures as HighPerformance Electrocatalysts for the Oxygen Evolution Reaction, Angew. Chemie Int. Ed. 58 (2019) 4227–4231.

[82] J. Wang, H.C. Zeng, Hybrid OER Electrocatalyst Combining Mesoporous Hollow Spheres of N, P-Doped Carbon with Ultrafine Co2NiOx, ACS Appl. Mater. Interfaces. 12 (2020) 50324–50332.

[83] Q. He, Y. Wan, H. Jiang, Z. Pan, C. Wu, M. Wang, X. Wu, B. Ye, P.M. Ajayan, L. Song, Nickel Vacancies Boost Reconstruction in Nickel Hydroxide Electrocatalyst, ACS Energy Lett. 3 (2018) 1373–1380.

[84] W. Chen, Y. Zhang, G. Chen, Y. Zhou, X. Xiang, K. “Ken” Ostrikov, Interface Coupling of Ni–Co Layered Double Hydroxide Nanowires and Cobalt-Based Zeolite Organic Frameworks for Efficient Overall Water Splitting, ACS Sustain. Chem. Eng. 7 (2019) 8255–8264.

[85] G. Li, L. Lu, L. Pei, Z. Ma, Y. Yuan, M.-L. Hu, Q. Miao, J. Zhong, In Situ Transformation of Metal–Organic Frameworks into Hollow Nickel–Cobalt Double Hydroxide Arrays for Efficient Water Oxidation, Inorg. Chem. 61 (2022) 738–745.

[86] X. Bai, Q. Wang, J. Guan, Bimetallic Iron–Cobalt Nanoparticles Coated with Amorphous Carbon for Oxygen Evolution, ACS Appl. Nano Mater. 4 (2021) 12663–12671.

[87] S. Zhao, Y. Wang, J. Dong, C.-T. He, H. Yin, P. An, K. Zhao, X. Zhang, C. Gao, L. Zhang, J. Lv, J. Wang, J. Zhang, A.M. Khattak, N.A. Khan, Z. Wei, J. Zhang, S. Liu, H. Zhao, Z. Tang, Ultrathin metal–organic framework nanosheets for electrocatalytic oxygen evolution, Nat. Energy. 1 (2016) 16184.

[88] K. Akamine, K. Morita, K. Sakai, H. Ozawa, A Molecular-Based Water Electrolyzer Consisting of Two Mesoporous TiO2Electrodes Modified with Metalloporphyrin Molecular Catalysts Showing a Quantitative Faradaic Efficiency, ACS Appl. Energy Mater. 3 (2020) 4860–4866.